scientific reports

Check for updates

OPEN

Renewable synthesis of MoO$_3$ nanosheets via low temperature phase transition for supercapacitor application

K. N. Amba Sankar[1✉], Lokesh Kesavan[2✉], Bikash Saha[3,4,8], M. K. Jyolsnaraj[5], S. Mohan[6], P. Nandakumar[1], Kallol Mohanta[5,7✉] & Carita Kvarnström[2✉]

2D transition metal oxides have created revolution in the field of supercapacitors due to their fabulous electrochemical performance and stability. Molybdenum trioxides (MoO$_3$) are one of the most prominent solid-state materials employed in energy storage applications. In this present work, we report a non-laborious physical vapor deposition (PVD) and ultrasonic extraction (USE) followed by vacuum assisted solvothermal treatment (VST) route (*DEST*), to produce 2D MoO$_3$ nanosheets, without any complex equipment requirements. Phase transition in MoO$_3$ is often achieved at very high temperatures by other reported works. But our well-thought-out, robust approach led to a phase transition from one phase to another phase, for e.g., hexagonal (*h*-MoO$_3$) to orthorhombic (*α*-MoO$_3$) structure at very low temperature (90 °C), using a green solvent (H$_2$O) and renewable energy. This was achieved by implementing the concept of oxygen vacancy defects and solvolysis. The synthesized 2D nanomaterials were investigated for electrochemical performance as supercapacitor electrode materials. The α-MoO$_3$ electrode material has shown supreme capacitance (256 Fg^{-1}) than its counterpart *h*-MoO$_3$ and mixed phases (*h* and *α*) of MoO$_3$ (< 50 Fg^{-1}). Thus, this work opens up a new possibility to synthesize electrocapacitive 2D MoO$_3$ nanosheets in an eco-friendly and energy efficient way; hence can contribute in renewable circular economy.

Nanometal oxide compounds have attracted considerable interest for the creation of advanced supercapacitors due to their capability to deliver pseudo-capacitance. Two dimensional (2D) nanostructures of transition metal oxides exhibit excellent performance in energy storage applications as they possess high fraction of surface exposed atoms. They have enhanced specific capacitance with better energy density compared to carbon nano-materials and good chemical stability than conductive polymers[1]. To utilize the potential of metal oxides in this context, it is crucial to regulate their electronic structure, electrical conductivity, and active sites. Introducing oxygen vacancies into metal oxides presents promising opportunities for enhancing these attributes. Therefore, a comprehensive overview of the latest advancements in this field is critically important[2].

Molybdenum compounds have so far have had a big impact on the world of 2D materials. Similar to graphite, it is layered and may be exfoliated or reconstructed into thin layers. Molybdenum trioxide (MoO$_3$) is one of the transition metal oxide material with unique physical and chemical characteristics such as phase transfer and charge transfer ability, cation accommodation efficiency, semi-conductance etc.[3], thus paving a way to various technological applications in recent times, such as, catalysts, gas sensors, supercapacitors, and batteries. MoO$_3$

[1]Department of Electronics, PSG College of Arts and Science, Coimbatore, Tamil Nadu 641014, India. [2]Department of Chemistry, Materials Chemistry, University of Turku, Henrikinkatu 2, 20014 Turku, Finland. [3]Solid State Physics Division, Bhabha Atomic Research Centre, Mumbai 400085, India. [4]Homi Bhabha National Institute, Anushakti Nagar, Mumbai 400 094, India. [5]Nanotech Research Innovation and Incubation Centre (NRIIC), PSG Institute of Advanced Studies, Avinashi Road, Coimbatore, Tamil Nadu 641004, India. [6]Physical and Materials Chemistry Division, CSIR-National Chemical Laboratory, Pune 411008, India. [7]Senior Research Scientist, Prophecy Sensorlytics LLC, GN4, Sector V, Salt Lake, Kolkata, West Bengal 700156, India. [8]Department of Physics and Astronomy, University of Missouri, 223 Physics Building, Columbia, MO 65211, USA. ✉email: ambasankarji@gmail.com; lokesa@utu.fi; kmohanta@gmail.com; carkva@utu.fi

has fascinating wide band gap and three existing polymorphs phases. These are low temperature metastable monoclinic (β-MoO_3), metastable hexagonal (h-MoO_3) and thermodynamically stable orthorhombic (α-MoO_3) structures[4-7].

Physical vapor deposition (PVD) is one of the important techniques to deposit MoO_3 on a chosen substrate because it produces highly crystalline and stratified structures with high yield[3]. In an oxygen-deficient environment, the reduction of MoO_3 gives rise to several phases of MoO_{3-x} (where $0 < x < 1$) with a ReO_3-type structure, such as Mo_9O_{26}, Mo_8O_{23}, and Mo_4O_{11}. These phases are categorized as part of the Magneli series, characterized by the composition Mo_nO_{3n-1}[8]. The phase transition in MoO_3 can be achieved through thermal treatments at above 350 °C[9]. h-MoO_3 can be obtained at 440 °C[10], whereas β-MoO_3 and stable α-MoO_3 phases can be obtained at 600 °C, 750 °C respectively[4]. Among these different phases, α-MoO_3 is getting more attention due to excellent catalytic activity and high electrochemical performance as reported in the literature[11].

Regulating the physicochemical properties through engineering of oxygen defects is a powerful approach to significantly alter materials' characteristics in a controlled manner. Generally, oxygen defects play a crucial role in the optical and electrical properties of transition metal oxide materials. In the case of oxygen-deficient MoO_{3-x}, the presence of oxygen vacancies leads to the formation of energy states within the forbidden optical band gap of the growing thin film, facilitated by the presence of excess molybdenum (Mo) atoms[12-14]. The presence of oxygen vacancies in interlayer spacing followed by phase transition, which in turn will reflect in superior specific surface area, electroactive sites, electrical conductivity. The intercalation offers two times higher pseudocapacitive behavior for MoO_{3-x} than MoO_3[15]. Hence, oxygen defect mediated phase transition is essential to study in developing desired application. However, these phase transitions are often carried out at high temperatures, thus consuming lot of thermal energy and energy costs. Hence, in overall, it is important to study cost effective, eco-friendly phase transitions to support renewable, recyclable processes.

Based on the prior literature knowledge on MoO_3 syntheses and characterizations, we decided to develop a facile method (**DEST**) in which we aimed to convert the commercially acquired bulk MoO_3 material into an amorphous (*am*-) MoO_{3-x} nanomaterial first, by physical vapor deposition (PV**D**), then ultrasonically extract (US**E**) this nanomaterial into suitable green solvents, which will be the resource feed for the phase transition of MoO_{3-x} that we tried to achieve at very low temperature under vacuum assisted solvothermal treatment (V**ST**) conditions. In this work, we report an oxygen defect mediated phase transition ($am \rightarrow h \rightarrow \alpha$ MoO_3) happening just at 60-90 °C, in water or *iso*-propanol, for the first time ever. VST can be done in rotary evaporation mode, which is a very basic technique to extract or remove solvents[16]. This simple, yet fruitive method is proposed for the potential use in the synthesis of metastable h-MoO_3, stable α-MoO_3 and mixed h and α-MoO_3 from pre-synthesized *am*-MoO_{3-x} solutions. Moreover, these crystalline phases of MoO_3 can be finetuned using an appropriate selection of solvents, and operating modalities like temperature, vacuum level, rotation speed etc., during VST. We also believe that our *DEST* synthesis approach could bring down enormous energy and waste solvent management costs while scaling up the production of 2D MoO_3 nanosheets. Further, we have characterized the *DEST*-synthesized materials to understand the effect of oxygen vacancies and the mechanism of phase transition. The postulates have been detailed using hypothetical premises. Finally, the as-synthesized crystalline phases of MoO_3 were subjected to a model application; supercapacitor performance, which is an auxiliary study in this work.

Our primary focus in the present work is to convey the larger message to the scientific community that the phase transition of MoO_3 polymorphs can be done at lower temperatures using green solvents without any sophisticated equipment requirements. For e.g., Jadkar et al. reported a method which employed CVD technique with the operation temperature of 1500 ± 50 °C[17]. In their method, 'Mo' filament was directly oxidized to α-MoO_3. Also, there was no scope of intermediate phase transitions like, from hexagonal phase (h-) and orthorhombic phase (α-). Han et al.'s method required an electrospinning equipment and again high temperature, up to 300 °C was needed to produce α-MoO_3 from its precursor[18]. Whereas, our work involves in converting amorphous MoO_{3-x} into h-MoO_3, α-MoO_3 and mixed phases (h and α) of MoO_3 at the maximum 60–90 °C using either water or *iso*-propanol in a simple vacuum distillation unit. The new insights we are aiming to provide here is the theoretical background of oxygen vacancies and its refilling by solvolysis, which can yield different crystalline phases of MoO_3 practically.

The other important reason why we study the phase transitions in MoO_3 crystal systems is that different phases of MoO_3 crystals could possess varying physico-chemical properties. Materials researchers would always want to exploit these properties, to suit their application that they are developing, for e.g., catalysis, adsorbents, composites, charge storage etc. Hence, we chose to carry out capacitance measurement studies in this present work. Making comparisons are part of research exercise. Thus, we compared the MoO_3 polymorphs for their electrochemical performance. As these polymorphs were prepared by a new route, we were inquisitive of knowing their electrochemical properties. We believe that our *DEST* synthesis approach could bring up new properties in the crystalline structure of 2D MoO_3 nanosheets. Therefore, it would offer a vibrant supercapacitor material in energy storage applications for the future. Also, our work can contribute to a renewable, circular economy in a longer run.

Results and discussion
Structural determination of MoO_3 polymorphs
DEST-synthesized MoO_3 samples such as (1) *am*-MoO_{3-x} solvolyzed at 60 °C in water (MO_{w60}), (2) *am*-MoO_{3-x} solvolyzed at 90 °C in water (MO_{w90}) and (3) *am*-MoO_{3-x} solvolyzed at 90 °C in *iso*-propanol (MO_{ipa90}) were subjected to detailed functional group analyses (FT-IR, Raman, UV–Vis, XRD, XPS), after their phase transition, to investigate the chemical bonding states between molybdenum and oxygen atoms.

FT-IR spectra (Fig. 1) confirmed that MO_{w60} and MO_{ipa90} were exhibiting almost similar characteristic responses like (i) a shallow peak at 3423 cm^{-1} corresponding to H–OH stretching vibration of firmly bounded water molecules in the sample[19], (ii) less intense peaks at 2916 cm^{-1}, 2845 cm^{-1} denoting C–H stretching, (iii) a prominent peak at 1612 cm^{-1} attributed to H–O–H bending vibration, (iv) then finger print region with some clear peaks at 970 cm^{-1}, 906 cm^{-1} due to stretching of Mo=O double bond vibrations of hexagonal phase[20], and a peak at 548 cm^{-1} due to single oxygen atom interaction with three molybdenum atoms[21] (Fig. 1). MO_{w60} and MO_{ipa90} samples having two peaks present at 2916 cm^{-1} and 2845 cm^{-1} were attributed to –CH_2 vibration[22] caused by any organic impurities in H_2O or *iso*-propanol.

On the other hand, MO_{w90} sample did not show any peaks at higher wavenumbers (from 3500 cm^{-1} to 1700 cm^{-1}) but at 1612 cm^{-1} and the finger print region, similar to MO_{w60} (Fig. 1). The finger print region in MO_{w90} was slightly blue shifted to (a) 987 cm^{-1}, (b) 864 cm^{-1}, (c) 601 cm^{-1}, and (d) 466 cm^{-1}, attributable to (a) Mo=O stretching vibration which is representing the stable, layered orthorhombic MoO_3 phase, (b) orthorhombic MoO_3 structure having Mo–O–Mo bonding with stretching vibrations of O_3 atoms[23], (c) Mo–O vibrations[21], (d) Mo_2–O_4 bonding due to solvolyzing H_2O molecules, respectively. From these results, it was confirmed that the samples MO_{w60} and MO_{ipa90} were in hexagonal crystalline structure (h-MoO_3) and MO_{w90} was in orthorhombic crystalline structure (α-MoO_3). In order to confirm the phase transition further, the Raman Spectroscopy was applied next.

The micro-Raman spectra of all three MoO_3 samples (MO_{w60}, MO_{w90}, MO_{ipa90}) were collected under 523 nm excitation and recorded in the range from 1100 to 100 cm^{-1} as shown in Fig. 2. The bands appeared between 100 to 400 cm^{-1} and 600 to 1000 cm^{-1} were representing bending, stretching vibrations of Mo–O/Mo=O. These are the lattice modes giving rise to the bands in lower region of MoO_6 octahedra in h-MoO_3 and α-MoO_3, respectively[24]. The peaks appeared from 100 to 300 cm^{-1} were due to the MoO_6 skeleton base structure, the peaks between 300 and 700 cm^{-1} were assigned to O–Mo–O bonds and the absorption at high wave number range, 700 to 1000 cm^{-1}, corresponded to Mo–O–Mo bonding. A well-defined sharp peak present at 820 cm^{-1}, along with other main peaks 666 and 993 cm^{-1} were reflecting the fingerprint region of the stable α-MoO_3 phase[24-26]. A tiny peak at 909 cm^{-1} present in MO_{w90}, MO_{ipa90} samples could be an indication of shared identity of a particular crystalline phase between these two samples. The detailed Raman vibrational analysis of bonds for h-MoO_3 and α-MoO_3 in comparison with literature evidences is shown in supplementary information file (SI); Tables S1 and S2. From this, the formation of h-MoO_3 (MO_{w60}, MO_{ipa90}) and α-MoO_3 (MO_{w90}) in our experimental conditions were confirmed. Further to determine the electronic states/band gaps in these polymorphs, the synthesized MoO_3 samples (MO_{w60}, MO_{w90}, MO_{ipa90}) were subjected to UV–Vis absorption spectroscopy.

The UV–Vis spectroscopic study, as illustrated in Fig. 3a, provides detailed insights into the optical properties of the samples, MO_{w60}, MO_{w90}, and MO_{ipa90}. A distinct excitonic absorption peak at 212 nm was observed in all three samples, indicating the presence of 2D MoO_3 nanosheets[27]. This characteristic excitonic absorption is a hallmark feature of 2D materials. Furthermore, additional band edge absorptions were observed at different wavelengths for each sample: 300 nm for MO_{w60} (h-MoO_3), 385 nm for MO_{w90} (α-MoO_3), and 315 nm for MO_{ipa90} (h-MoO_3). These characteristic absorption wavelengths indicated variations in the electronic properties and band structures in these samples. Thus, confirming different phases of MoO_3. Figure 3b showcases the determination of band gaps (E_g) through Tauc plot analysis using the UV–Vis spectrum. The calculated E_g values for MO_{w60}
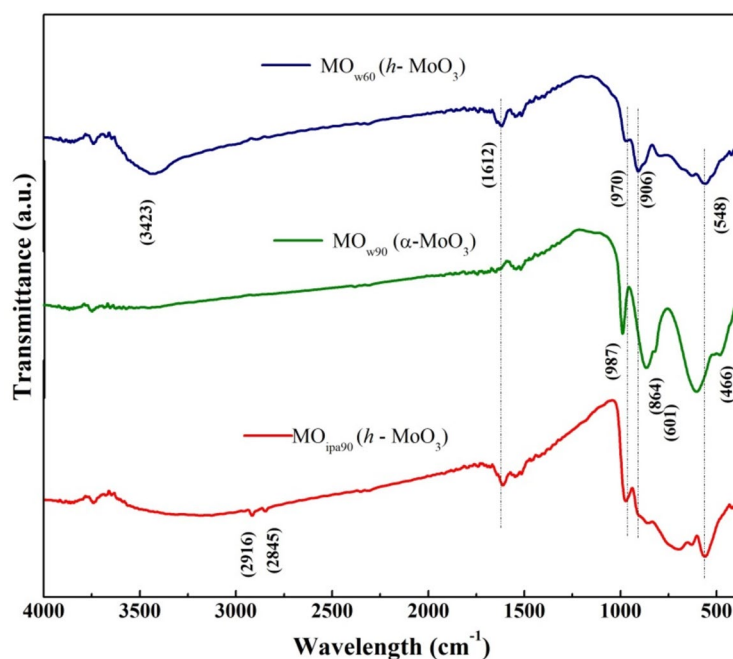

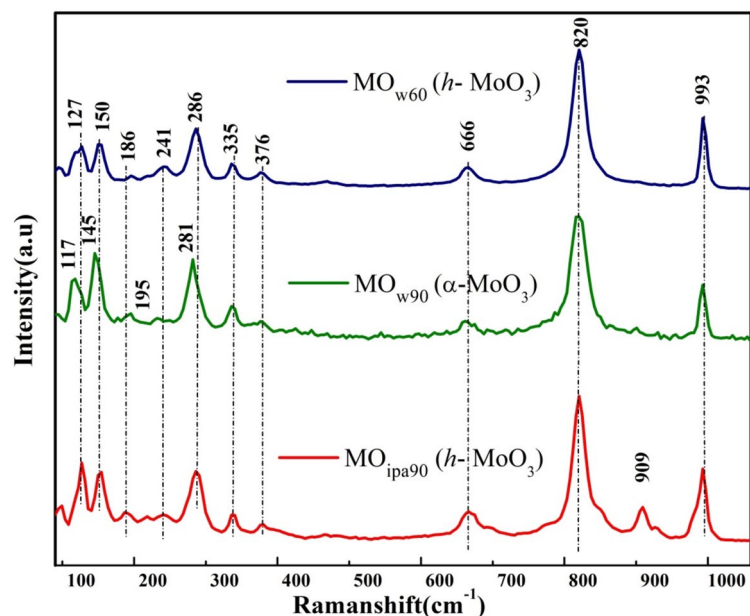**Figure 1.** FTIR spectra of *DEST*-made MoO_3 polymorphs materials.

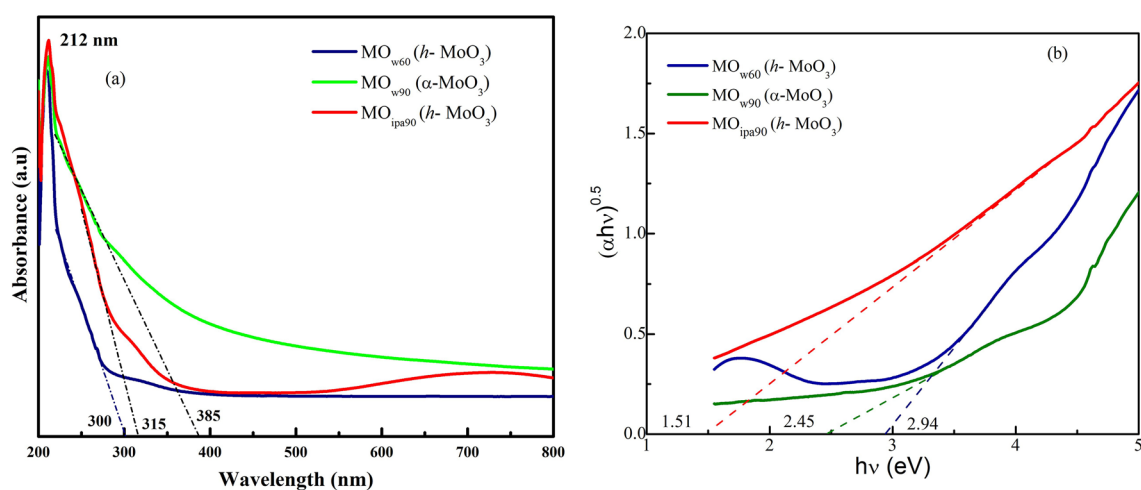**Figure 2.** Raman spectra of *DEST*-made MoO₃ polymorphs materials.

Figure 3. UV–Vis spectra of *DEST*-made MoO₃ polymorphs materials. (**a**) Absorbance spectra, (**b**) Tauc plot for finding E_g.

(h-MoO₃), MO$_{w90}$ (α-MoO₃), and MO$_{ipa90}$ (h-MoO₃) were 2.94 eV, 2.45 eV, and 1.51 eV respectively. These values did match with those values reported in literature by Lei Zheng et al.[10], Hanmei Hu et al.[28], and Yuehong Song et al.[29], providing validation for the accuracy of the experimental measurements.

However, some more clarity was needed to distinguish MO$_{w60}$ from MO$_{ipa90}$ as though they showed similar IR, Raman spectral lines, their UV–Vis spectral data revealed that there were some minute variations between them. Also, in Raman Spectroscopic data, there was an ambiguity in identifying crystalline phases, as all three samples showed the distinct peaks at 666 cm⁻¹, 820 cm⁻¹ and 993 cm⁻¹. To sort this out, we went for an extensive crystal structural analysis of these MoO₃ polymorphs using XRD technique.

Crystal structural analysis of MoO₃ phases

The most important analysis to prove the phase transition in as-synthesized MoO₃ samples was X-ray diffraction studies (XRD). Figure S1 shows the XRD patterns of commercially purchased stock MoO₃ (bulk powder), physical vapor deposited MoO₃₋ₓ (nanopowder), and then recrystallized MoO₃ samples from water (MO$_{w60}$, MO$_{w90}$) and isopropanol (MO$_{ipa90}$), along with simulated diffraction patterns of h-MoO₃ and α-MoO₃. This direct comparison allowed us to assess the peak positions and intensities of the corresponding phases.

The thin films of MoO₃ (thickness of 150 nm) deposited on glass substrates by PVD, are usually amorphous and sub-stoichiometric (am-MoO₃₋ₓ) in nature. The absence of sharp peaks and presence of broad hump (26.17°) in the XRD pattern confirmed the amorphous (am-) nature of as-deposited thin films (Fig. S1). This hump was

due to weak diffraction, suggesting that the film possesses a combination of amorphous and crystalline characteristics (64% amorphous and 36% crystalline).

The crystallinity percentage was calculated using the following formula;

$$\text{Crystallinity (\%)} = \frac{\text{Area of crystalline peaks}}{\text{Area of crystalline peak} + \text{Area of amorphous peak}} \times 100$$

Contrary to am-MoO_{3-x}, the recrystallized MoO_3 samples; MO_{w60}, MO_{w90}, MO_{ipa90}, were exhibiting sharp distinct peaks in the XRD pattern, suggesting phase transition and enhanced crystallinity (Fig. S1, 4). The samples recrystallized using water (MO_{w60}) exhibited a phase transition from amorphous (am-MoO_{3-x}) to hexagonal structure (h-MoO_3). However, with an increase in recrystallization temperature (MO_{w90}), a complete phase transition from amorphous (am-MoO_{3-x}) to thermodynamically stable orthorhombic structure (α-MoO_3) was observed. We also believe that this transition should have happened via the intermediate, which is metastable h-MoO_3 form, as we already know that h- structure was the resultant phase at 60 °C in H_2O. Conversely, in the case of MoO_3 sample recrystallized using iso-propanol (MO_{ipa90}), a mixed phases of h and α- MoO_3 product was obtained, suggesting an initial phase transition from am-MoO_{3-x} to h-MoO_3, followed by a partial phase transition from h-MoO_3 to α-MoO_3 occurred in this sample. The measured diffraction patterns of MoO_3 phases were analyzed by using the Rietveld refinement technique (assisted by FULLPROF computer program).

The Rietveld analysis of the XRD of MO_{w60} sample, synthesized at 60 °C in H_2O, revealed a pure single-phase of h-MoO_3, confirmed by the space group P 63/m and space group number 176 (Fig. 4a). This analysis counted the lattice parameters of h-MoO_3 as follows: $a = b = 10.6133(2)$, $c = 3.7243(3)$, $\alpha = \beta = 90°$, and $\gamma = 120°$. The fractional coordinates of the atomic positions are presented in Table S3.

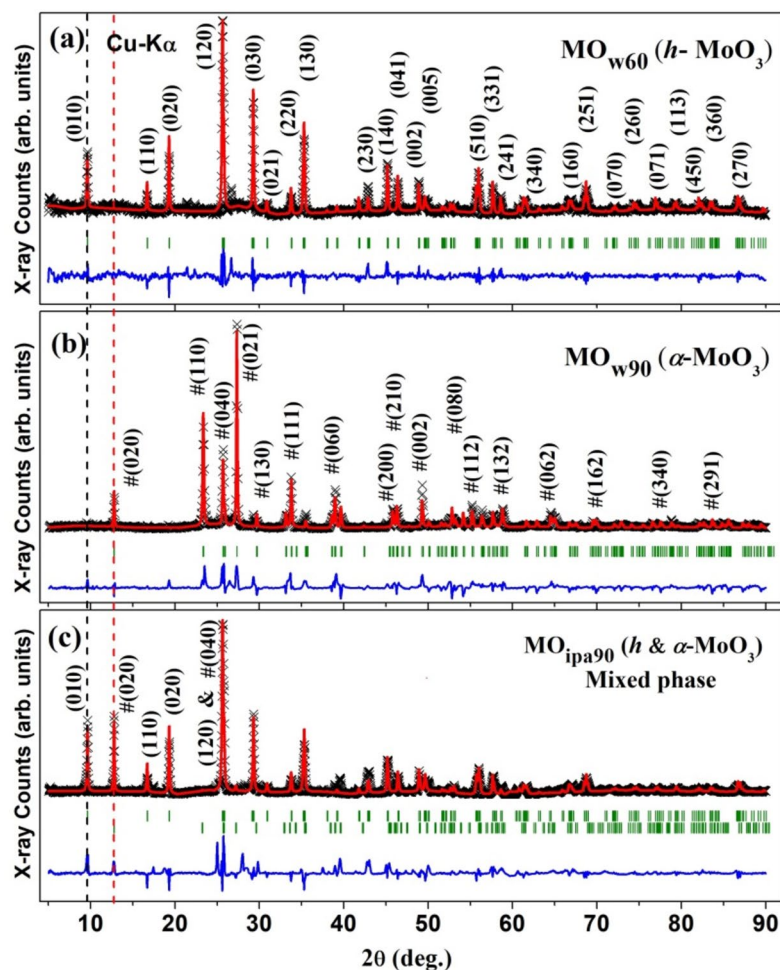**Figure 4.** X-ray diffraction patterns refined by Rietveld method for *DEST*-made MoO_3 polymorphs materials: (**a**) MO_{w60} (h-MoO_3), (**b**) MO_{w90} (α-MoO_3), (**c**) MO_{ipa90} (mixed phases of h and α-MoO_3). Black and red lines (through the data points) are representing the experimental and the calculated patterns, respectively. The difference between the experimental and the calculated patterns is shown by the blue lines at the bottom of each panel. The vertical green bars represent the allowed nuclear Bragg positions.

This analysis further revealed that the Mo ions reside in octahedral arrangement with the O atoms (Fig. 5a) and no monoclinic β-MoO$_3$ structure (Fig. 5b) was obtained with any of the synthesized samples (MO$_{w60}$, MO$_{w90}$, MO$_{ipa90}$). The hexagonal crystalline structure (h-MoO$_3$) of the MO$_{w60}$ sample possess 1D tunnels along crystallographic c-axis, which is made up of the zigzag chains of MoO$_6$ octahedra, the very building block of the crystal (Fig. 5c).

The Rietveld analysis of the XRD of MO$_{w90}$ sample, synthesized at 90 °C in H$_2$O, showed again a single-phase, which is thermodynamically stable orthorhombic crystal symmetry (α-MoO$_3$), confirmed by the space group P n m a (Fig. 4b). The lattice parameters of α-MoO$_3$ phase were found to be a = 3.9591(2), b = 13.8611(6), c = 3.7243(3), $\alpha = \beta = \gamma = 90°$. The fractional coordinates of the atomic positions are presented in Table S3. The orthorhombic structure of α-MoO$_3$ consists of layered planes of the foundational octahedron (oh-MoO$_6$) units, in double layer form (Fig. 5d). These stacked bilayers of distorted MoO$_6$ octahedral units arranged in an ABAB… pattern with edge-sharing zigzag rows and corner-sharing rows, along the [001] and [100] directions.

The Rietveld analysis of the XRD of MO$_{ipa90}$ sample, synthesized at 90 °C in iso-propanol ((CH$_3$)$_2$CHOH) confirmed the presence of (010) and #(020) of h-MoO$_3$ and α-MoO$_3$ phases respectively (Fig. 4c), indicating the composition of mixed phases, but predominantly composed of h-MoO$_3$ (space group P 63/m and space group number 176). This analysis (considering both phases) further suggested that the mixed phase contains 72.6% of h-MoO$_3$ and 27.4% of α-MoO$_3$. The refined crystal structural parameters of mixed phase are as follows (Table S4): a = b = 10.6134(2), c = 3.7207(3), $\alpha = \beta = 90°$, and $\gamma = 120°$ for h-MoO$_3$, and a = 3. 9832(3), b = 13.8673(5), c = 3.7192(4), $\alpha = \beta = \gamma = 90°$ for α-MoO$_3$.

Thus, the XRD measurements have confirmed the phase transitions occurred in as-synthesized MoO$_3$ samples, very lucidly and proved that they are polymorphs. XRD data also nullified the ambiguity that we had from UV–Vis and Raman spectral data, that (i) whether the phase change happened in MO$_{w60}$ and MO$_{ipa90}$ are same or not, and (ii) the formation of α-MoO$_3$ in MO$_{w90}$. Henceforth, we mark the polymorph of MO$_{ipa90}$ as 'h and α-MoO$_3$' instead of just 'h-MoO$_3$'. Therefore, the facile vacuum assisted solvothermal (VST) approach has yielded a very nice phase transition ($am \rightarrow h \rightarrow \alpha$) even at very low temperature in the presence of a protic, green solvent like water.

Surface morphology and topography analysis

The h-MoO$_3$ and α-MoO$_3$ represent two distinct polymorphs of MoO$_3$ with unique structural and electronic properties. Understanding their surface morphology and topography is crucial for exploring their potential applications further. High Resolution Transmission Electron Microscopy (HRTEM) analysis was employed to understand the surface morphology and crystal structure of MoO$_3$ polymorphs synthesized by DEST method. Images of low magnification, lattice fringes and SAED pattern of the materials (MO$_{w60}$, MO$_{w90}$, MO$_{ipa90}$) are shown in Fig. 6. All the samples were showing a two-dimensional structure in few hundreds of nanometer size. The interplanar spacing analysis of MoO$_3$ polymorphs, conducted in lattice fringe images of HRTEM provides crucial insights into the material's structural characteristics at the atomic level. By measuring the distances
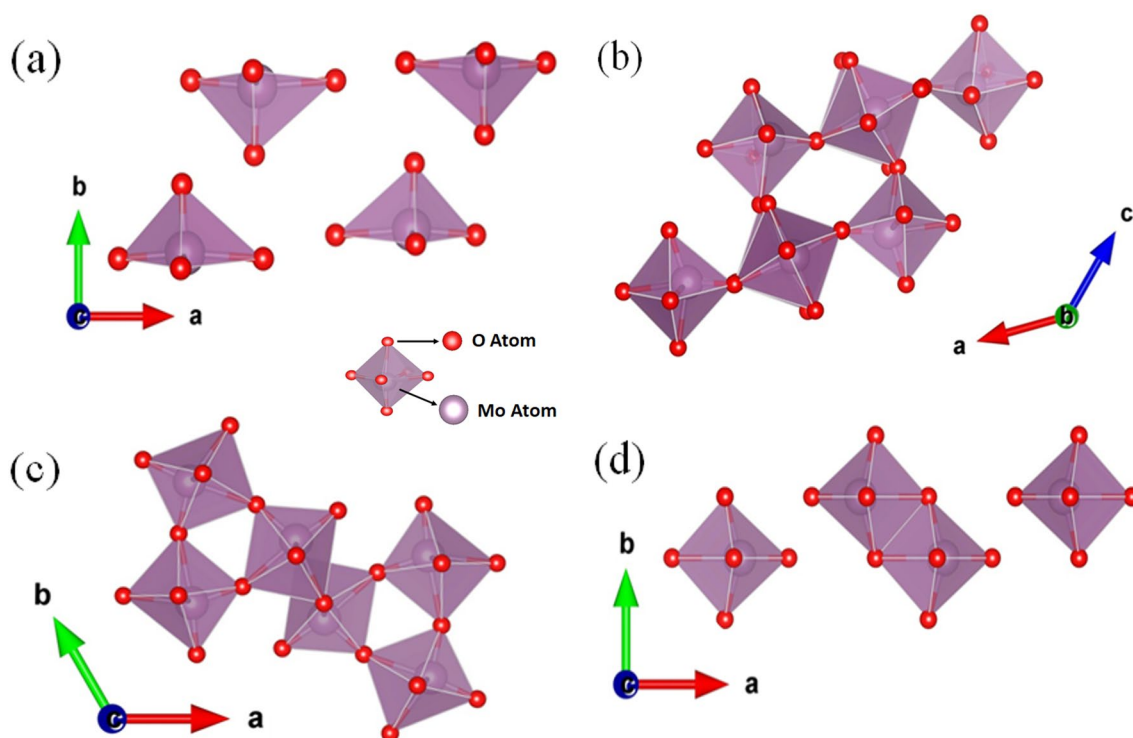

Figure 5. A model unit cell crystal structure of (**a**) MoO$_3$, (**b**) β-MoO$_3$, (**c**) h-MoO$_3$ and (**d**) α-MoO$_3$.
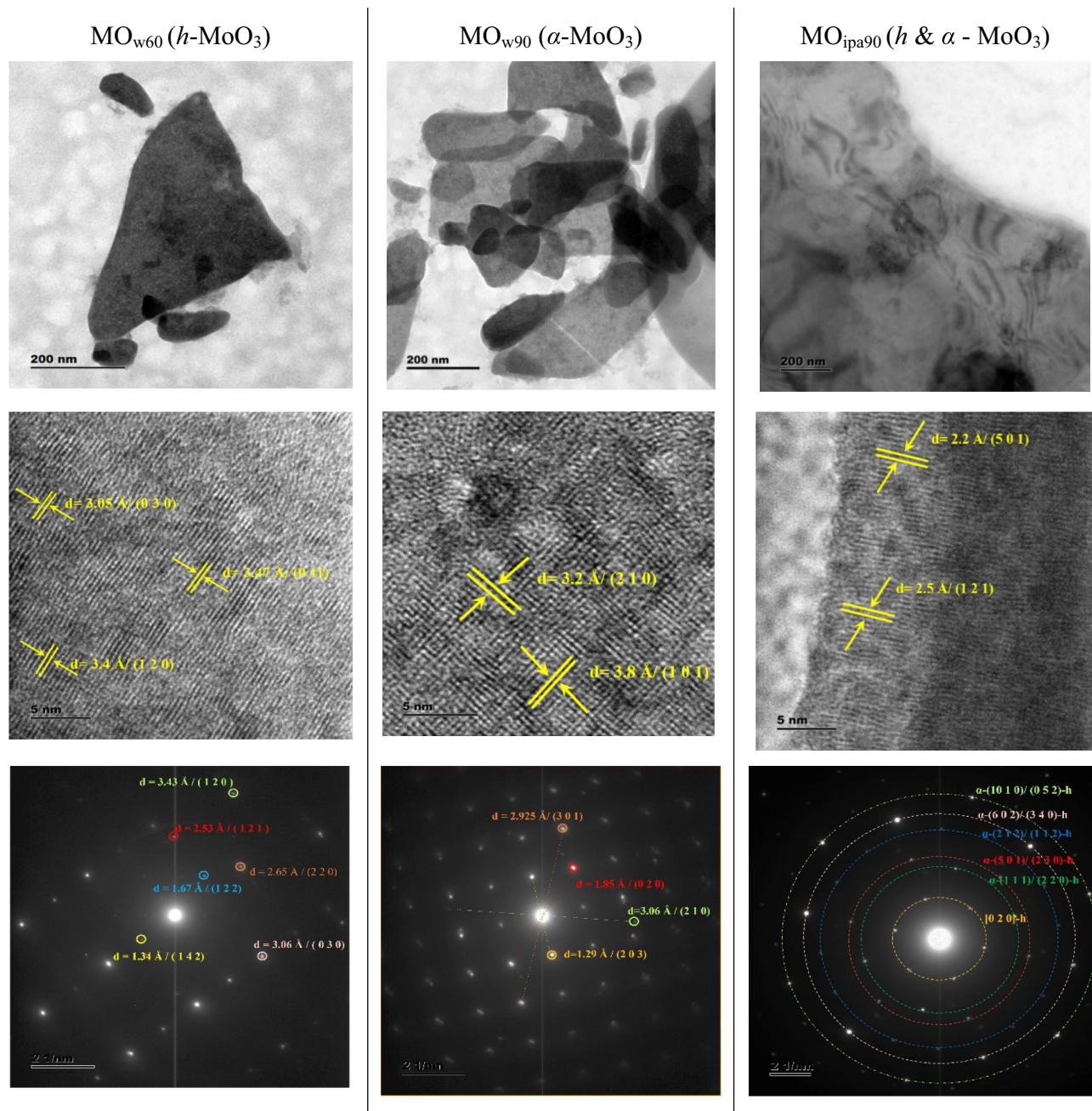
Figure 6. HRTEM images of *DEST*-made MoO$_3$ polymorph 2D nanosheet materials.

between adjacent crystal planes along various crystallographic directions, the arrangement of atoms within the MoO$_3$ lattice can be understood.

The obtained interplanar spacing results for hexagonal molybdenum trioxide (*h*-MoO$_3$) of MO$_{w60}$, were d = 3.47 Å (011), d = 3.4 Å (120), and d = 3.05 Å (030). These (011), (120), and (030) planes confirmed the unique arrangement of atoms within the hexagonal lattice of MoO$_3$. The orthorhombic molybdenum trioxide (*α*-MoO$_3$) of MO$_{w90}$ exhibited interplanar spacings of d = 3.2 Å (210) and d = 3.8 Å (101). The interplanar spacing of 3.2 Å along the (210) crystallographic plane indicated the short distance between adjacent planes oriented in this direction, revealing the compact nature of the atomic arrangement within this plane. Conversely, the interplanar spacing of 3.8 Å along the (101) plane signified a larger separation between adjacent planes. These findings shed light on the anisotropic nature of *α*-MoO$_3$, where the interplanar spacings vary along different crystallographic directions. The mixed-phases of MO$_{ipa90}$ (*h* and *α*-MoO$_3$) showed interplanar spacings of d = 2.2 Å (501) and d = 2.5 Å (121), which was smaller than what pure, single phase *h*-MoO$_3$ and *α*-MoO$_3$ showed.

The bright pointed diffraction spots appeared in Selected Area Electron Diffraction (SAED) pattern confirmed high order of crystallinity in all three samples (MO$_{w60}$, MO$_{w90}$, MO$_{ipa90}$) (Fig. 6). From SAED pattern, the crystalline phases of MO$_{w60}$, MO$_{ipa90}$, were confirmed as hexagonal (*h*-MoO$_3$) structure. On the other hand, MO$_{w90}$ was confirmed to be orthorhombic (*α*-MoO$_3$) crystal structure. The samples showed different types of

lattice fringes with respect to oxygen defects formed during heat treatments (w60, w90, ipa90) under vacuum. The crystal structures of MoO_3 became irreversibly distorted as oxygen was removed initially from the lattice structure, followed by its refilling and the intercalation of H^+ ions from solvents[30,31]. This proved our claim again that the *DEST* method could efficiently bring a phase transformation even at very low temperature providing optimized solvothermal conditions (VST) are used.

Further, we have also investigated the microscopic visuals of 2D nanosheets of h-MoO_3 (MO_{w60}), α-MoO_3 (MO_{w90}) and mixed phases (h and α-MoO_3) of MO_{ipa90}, using SEM and AFM techniques as shown in Figs. 7a–c and 8 respectively.

The scanning electron microscopy (SEM) images clearly revealed sheet-like structures with diameters ranging from 1 to 2 microns for all the samples, effectively suggesting two-dimensional (2D) morphology (Fig. 7). Also, the images suggested that the sheets were formed uniformly in dimension, thus our synthesis method offers the feasibility of controlling the dimensions of the MoO_3 polymorphs at the micron scale level. This observation highlights the successful fabrication of MoO_3 polymorphs in our desired 2D form which holds significant implications in potential applications. Figure 8 illustrates AFM images of MoO_3 polymorphs. AFM imaging provided a high-resolution representation of the topography of the samples; MoO_3 nanoparticles. From the images, we can clearly see the individual nanoparticles appearing as distinct features on the substrate. This allows us to determine the size, shape and arrangement at the nanoscale.

Further, the oxidation states of Mo in the material and chemical bonding in the surface of samples (MO_{w60}, MO_{w90}, MO_{ipa90}) were investigated by the X-ray Photoelectron Spectroscopy (XPS) (Fig. 9a, b). The full energy
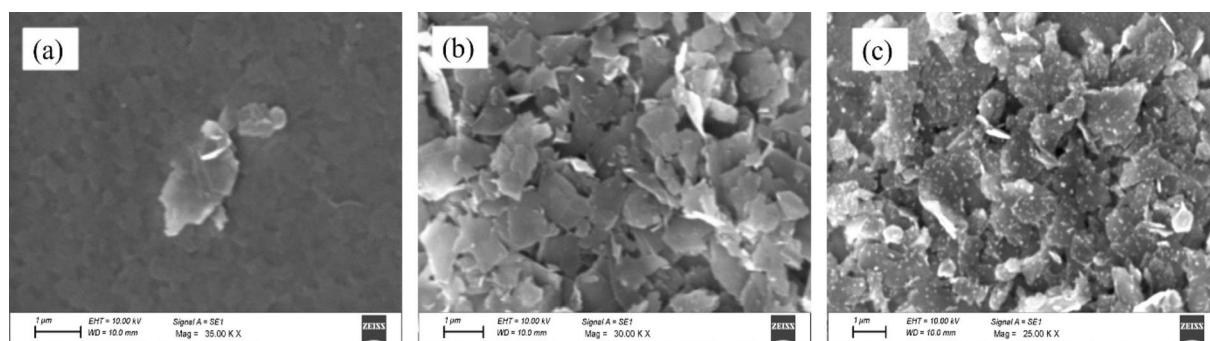

Figure 7. SEM images of *DEST*-made MoO_3 polymorph 2D nanosheet materials: (**a**) MO_{w60} (h-MoO_3), (**b**) MO_{w90} (α-MoO_3), (**c**) MO_{ipa90} (h and α-MoO_3).
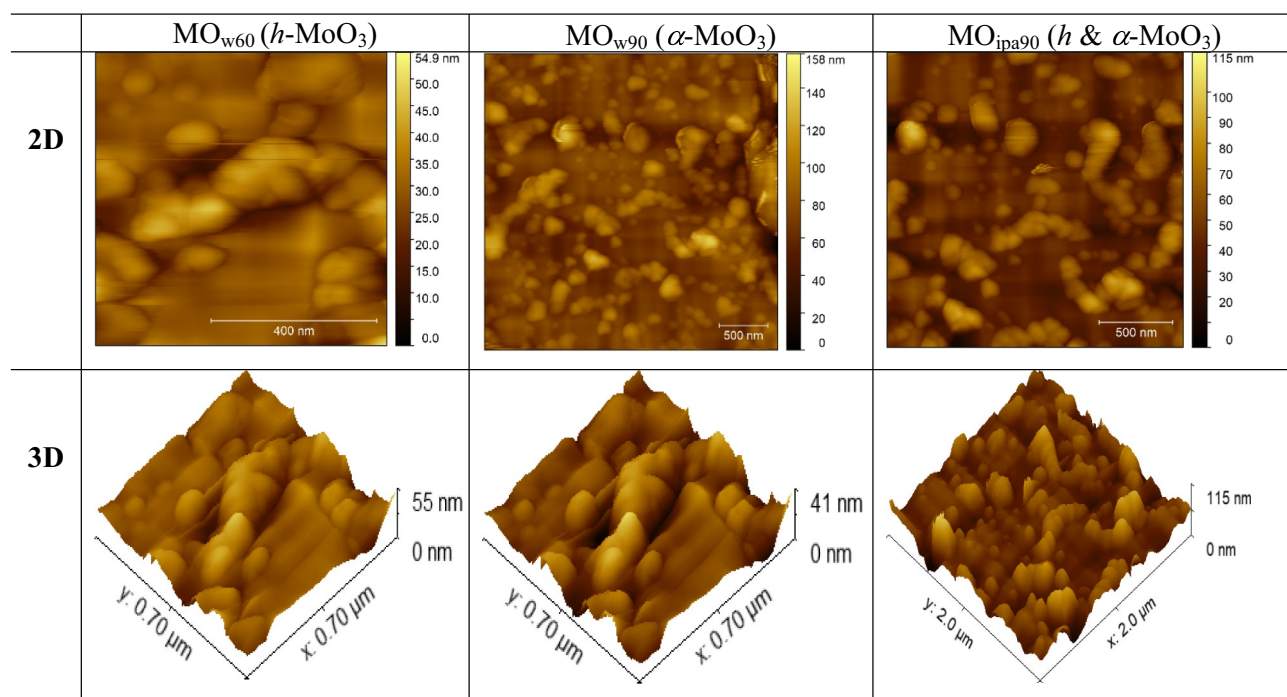

Figure 8. AFM images of *DEST*-made MoO_3 polymorph 2D nanosheet materials: (**a**) MO_{w60} (h-MoO_3), (**b**) MO_{w90} (α-MoO_3), (**c**) MO_{ipa90} (h and α-MoO_3).
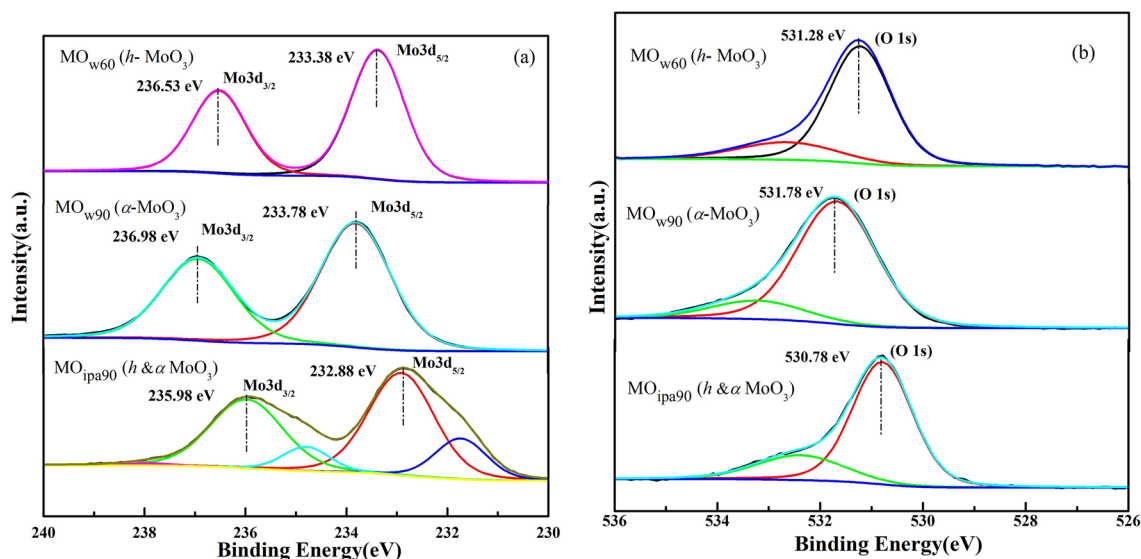
Figure 9. XPS spectra of *DEST*-made MoO$_3$ polymorph 2D nanosheet materials (**a**) Mo-3d core level region, (**b**) O-1s region.

survey spectrum (Fig. S2) of MoO$_3$ polymorphs confirmed the presence of Mo^{4p}, Mo^{3d}, C^{1s}, Mo^{3p} and O^{1s} peaks at their characteristic binding energies that validated the identity of MoO$_3$ in the sample.

In Fig. 9a, the deconvolution of the Mo spectrum scan revealed distinct peaks at (236.53 eV, 233.38 eV)[32,33], and (236.98 eV, 233.78 eV)[19,32,34], for MO$_{w60}$ and MO$_{w90}$ respectively. These peaks correspond to the spin–orbit doublets (3d$_{5/2}$ and 3d$_{3/2}$) of Mo^{6+}, thereby confirming the presence of MoO$_3$. However, these peaks slightly shifted to low binding energies (235.98 eV, 232.88 eV) for MO$_{ipa90}$[6,10,35,36]. This shift is due to subtle differences in the local chemical environment which influences the binding energies of Mo-related peaks in the XPS spectra[37,38]. O-1s peaks (Fig. 9b) also showed similar shift (531.28 eV, 531.78 eV, 530.78 eV for MO$_{w60}$, MO$_{w90}$, MO$_{ipa90}$), indicating variations in the oxygen bonding environment among different polymorphs.

To be specific, Table S5 shows that the Mo-3d$_{3/2}$, Mo-3d$_{5/2}$, O-1s peak positions, shifted 0.45 eV. 0.40 eV, 0.5 eV respectively, between the metastable *h*- and most stable *α*- phases of MoO$_3$. Similarly shifts of 0.55 eV, 0.50 eV, 0.50 eV noticed for the same peaks correspondingly, between the metastable *h*- and mixed phases (*h* and *α*-MoO$_3$) of the material. Further clear shifts of 1 eV, 0.9 eV, 1 eV were observed for the above-mentioned peaks respectively, between the most stable *α*-phase and mixed phases (*h* and *α*-MoO$_3$) of the material. Overall, the changes in surface chemistry alter the electron density near the surface, influencing the binding energies of photoelectrons, which resulted in XPS peak shifts.

We believe that *iso*-propanol mediated vacuum assisted solvothermal step (VST) could have caused different oxygen defect in MoO$_3$ than the water mediated synthesis. Oxygen defect creates low valent Mo ions, if these low valent ions haven't regenerated into Mo^{6+} completely, that could cause a slight shift in the binding energy. We also knew that the MO$_{ipa90}$ produced mixed phases of *h*-MoO$_3$ and *α*-MoO$_3$, thus *iso*-propanol acts very differently from water which produced solely the *α*-MoO$_3$ at 90 °C.

Hypothetical insights into the mechanism of phase transition in MoO$_{3-x}$ (*am→h→α*-MoO$_3$) under VST conditions

Our aim was to achieve the phase transition at very low temperature using physico-chemical method rather than widely reported high temperature-physical methods. In physical methods, MoO$_3$ is annealed at very high temperature (300–1500 °C) in flow furnaces or chambers, for its phase transition. Thus, consumes lot of energy during its production. We wanted to bring down this energy cost, by introducing a vacuum assisted solvothermal treatment (VST), where careful application of solvent can do a phase transition wonder. This very unique approach and the results, motivated us to discern the mechanistic details based on hypothetical premises.

In our studies, defects implantation has been adopted as a nuanced technique for modifying the crystalline phase and its physico-chemical properties, in order to achieve desired energy storage application from it. Defects created in various locations of the lattices, could adjust band structure, electron density and bonding at different degrees. Oxygen vacancies, a kind of intrinsic defect in metal oxides, is one of the most preferred fine tuning at crystal level, in materials designing. Through controlled removal of oxygen atoms from the lattices of metal oxides, the lattices become disordered and low valence metal ions are created. Further, these low-valent metal ions will look for foreign ions or oxygen atoms present in the solution/environment to make new bonding to stabilize themselves. So that, the free energy of the crystal system can be brought down, for better stability. Thus, paving a way for phase transition in the crystalline materials. This will have a major impact on the crystal structure and its inherent characteristics[39].

Oxide materials are highly prone to induced oxygen vacancy defects, especially when the metal ions are at higher oxidation state. In our case (MoO$_3$), the Mo is at +6 oxidation state, that can be reduced to lower oxidation

states, e.g., +4, by creating oxygen vacancies in thermal or chemical environment. It is well-known fact that MoO_3 could lose oxygen if it is heated under vacuum or other reducing environment conditions. Under these conditions, it should be noted that MoO_3 can quickly break down into lesser oxides[40–42], where the stoichiometry deviates from the ideal MoO_3 composition into MoO_{3-x}, due to the absence of oxygen atoms. These lesser oxides are known to have empirical compositions between MoO_3 and MoO_2, leading to the formation of low valent Mo^{4+} ions. Further, these low valent Mo^{4+} ions can be stabilized by supplying protons and the oxygen vacancies can be refilled by some fractions of oxygen from the protic solvents (Brønsted acids), to get back MoO_3. This was the theoretical basis of our experiment and we supplied protons (H^+) as foreign ions from water and *iso*-propanol, to quench the Mo^{4+} ions, for the regeneration MoO_3 with modified phase.

In this present work, we believe that the vacuum environment during PVD step, could have created some oxygen vacancies (Vo^i) already, with the formation of sub-stoichiometric molybdenum oxide, MoO_{3-x} (150 nm thickness), but without crystallinity (Fig. S1). Hence, to complete the recrystallization, we have taken the VST approach, after the MoO_{3-x} extraction step (USE). During VST also, there might be a creation of oxygen vacancies (Vo^{ii}) due to vacuum, with the formation of $MoO_{3-(x+y)}$. If the thickness of the MoO_{3-x} thin film deposition increased up to 350 nm, then positively charged structural defects would also increase due to the concentration of oxygen vacancies[43–45].
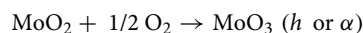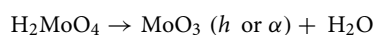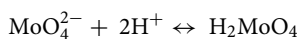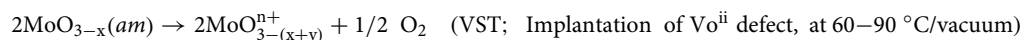
We denote these oxygen vacancies as,

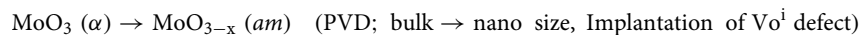(1) Vo^i—Primary oxygen vacancies: Intermediate—amorphous (*am-*) MoO_{3-x}, x—fraction of oxygen defected created during PVD.
(2) Vo^{ii}—Secondary oxygen vacancies: Intermediate—$MoO_{3-(x+y)}$; y—fraction of oxygen defected during VST.

Later, these oxygen defective intermediates were oxygen refilled to some extent and stabilized by protons through thermo-solvolysis at VST step. In VST, we have chosen the primary protic solvent, H_2O, as our reagent, which is green (eco-friendly, low cost, renewable) in nature. In order to evaluate its comparative performance, we have also employed *iso*-propanol (($CH_3)_2CHOH$), another weak protic solvent for solvolysis. In general, water is a highly polar solvent, which makes it effective for dissolving ionic compounds and facilitating reactions involving charged species. Many oxidation reactions are thermodynamically favorable in aqueous environments due to the high dielectric constant and hydrogen bonding capabilities of water. These properties stabilize charged intermediates and transition states, lowering the activation energy barrier for the reaction. After the oxidation reaction, water can be easily separated from the reaction mixture by distillation, evaporation, or other separation techniques. This simplifies product purification and reduces processing costs. *iso*-propanol is also a moderately polar solvent which can dissolve both polar and non-polar substances and again can stabilize the intermediates through hydrogen bonding or solvation effects, thereby influencing the reaction pathway and product distribution. Here, we mostly rely on the Brønsted–Lowry acidity and dissociation constant of the solvents to impact the hydrolysis of oxides.

The vacuum assisted heating (VST) creates the secondary oxygen defects followed by proton-hungry molybdate anions (MoO_4^{2-}) in the presence of these low-boiling solvents. What these solvents basically do is that, they push/shift the reaction equilibrium towards the right side of the equation, thereby inducing the formation of these anion intermediates according to Le Chatelier's principle of chemical equilibrium. Thus, we end up with regeneration of MoO_3 from the decomposition of molybdic acid, but with modified phase. Based on the product materials' characterization results, it was confirmed that water mediated VST did yield a successful phase transition ($am \rightarrow h \rightarrow \alpha$) in MoO_{3-x}, whereas *iso*-propanol mediated VST delivered a partial phase transition ($am \rightarrow h \rightarrow h$ and α), leaving a mixed phase product material. However, both the solvents yielded phase transition from $am \rightarrow h$ in MoO_{3-x} thoroughly and effectively.

We reasoned out that the physico-chemical properties of solvents play a major role in facilitating phase transition in MoO_{3-x} during VST. For e.g., Water is a more protic solvent than *iso*-propanol, because it has ten thousand times higher dissociation constant (H_2O: $K_a = 1 \times 10^{-14}$) than *iso*-propanol (($CH_3)_2CHOH$): ($K_a = 1 \times 10^{-18}$). Hence, water would release more protons in a short span of time, which is needed for the phase transition in MoO_{3-x}.
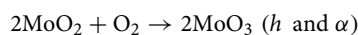
The following equations show a possible hydrolysis reaction between water and MoO_{3-x} containing oxygen vacancy, based on literature[46].

$$MoO_3 \ (\alpha) \rightarrow MoO_{3-x} \ (am) \quad (\text{PVD}; \ \text{bulk} \rightarrow \text{nano size, Implantation of } Vo^i \text{ defect})$$

$$2MoO_{3-x}(am) \rightarrow 2MoO_{3-(x+y)}^{n+} + 1/2 \ O_2 \quad (\text{VST}; \ \text{Implantation of } Vo^{ii} \text{ defect, at } 60-90 \ °C/\text{vacuum})$$

$$2MoO_{2.5}^{1+} + H_2O \leftrightarrow MoO_4^{2-} + MoO_2 + 2H^+ \quad (K_a = 1 \times 10^{-14})$$

$$MoO_4^{2-} + 2H^+ \leftrightarrow H_2MoO_4$$

$$H_2MoO_4 \rightarrow MoO_3 \ (h \text{ or } \alpha) + H_2O$$

$$MoO_2 + 1/2 \ O_2 \rightarrow MoO_3 \ (h \text{ or } \alpha)$$

According to the above equations, the commercially acquired bulk α-MoO_3 material was initially converted into an amorphous (*am-*) MoO_{3-x} nanomaterial, with implanted primary oxygen vacancies (Vo^i), at the initial

PVD step. Then, these am-MoO_{3-x} nanomaterials were ultrasonically extracted (USE) and subjected to VST for implanting secondary oxygen vacancies (Vo^{ii}), followed by the formation of a $(MoO_{3-(x+y)})^{n+}$ cation. This cation immediately got stabilized itself by reacting with solvent environment (H_2O) to form intermediates like MoO_2 and molybdate anion (MoO_4^{2-}). Further this anion reacted with available protons to produce less stable molybdic acid followed by its decomposition into molybdenum trioxide, with a new crystal phase (hex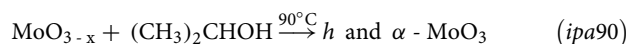agonal h-MoO_3 or orthorhombic α-MoO_3). The by-product MoO_2 also reacted with left over oxygen atoms to produce MoO_3 with new phase.

In the case of iso-propanol, it released protons slowly or produced lesser number of protons in the medium as its dissociation was weak. Hence, the solvation of $(MoO_{3-(x+y)})^{n+}$ cation was also slow and weak. Because of the inadequate concentration of released protons (H^+) in the medium, the hydrolysis of molybdate anions into molybdic acid, followed by its decomposition into α-MoO_3 was only achieved partially according to the stoichiometric equations mentioned below. Therefore, the product was the mixed phases of h and α-MoO_3, but dominated by h-phase as evidenced by XRD.

$$MoO_3 \ (\alpha) \rightarrow MoO_{3-x} \ (am) \quad (\text{PVD; bulk} \rightarrow \text{nano size, Implantation of } Vo^i \text{ defect})$$

$$4MoO_{3-x} \ (am) \rightarrow 4MoO_{3-(x+y)}^{n+} + O_2 \quad (\text{VST; Implantation of } Vo^{ii} \text{ defect, at 90 °C/vacuum})$$

$$4MoO_{2.5}^{1+} + 2(CH_3)_2CHOH + O_2 \leftrightarrow 2MoO_4^{2-} + 2MoO_2 + 4H^+ + 2(CH_3)_2C=O \ldots \left(K_a = 1 \times 10^{-18}\right)$$

$$2MoO_4^{2-} + 4H^+ \leftrightarrow 2H_2MoO_4$$

$$2H_2MoO_4 \rightarrow 2MoO_3(h \text{ and } \alpha) + 2H_2O$$

$$2MoO_2 + O_2 \rightarrow 2MoO_3 \ (h \text{ and } \alpha)$$
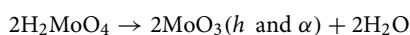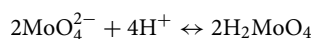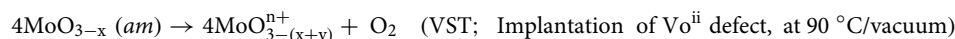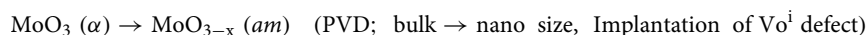
Therefore, the release of protons from solvent dissociation was the rate determining step in both the case of water and iso-propanol, which largely affected the intermediate and final product formation with phase transition.

$$MoO_{3-x} + H_2O \xrightarrow{60°C} h\text{-}MoO_3 \qquad (w60)$$

$$MoO_{3-x} + H_2O \xrightarrow{90°C} \alpha\text{-}MoO_3 \qquad (w90)$$

$$MoO_{3-x} + (CH_3)_2CHOH \xrightarrow{90°C} h \text{ and } \alpha\text{-}MoO_3 \qquad (ipa90)$$

We realize that our reasoning behind solvent-mediated mechanism is only at theoretical level and not experimentally proven yet. To negate this shortcoming, we will be doing in-situ spectroscopic measurements to understand the stoichiometric chemistry, reaction kinetics, and mechanism of this phase transition, in our future studies. These experiments will reveal the nature and distribution of oxygen vacancies, nature of intermediates, solvation level, proton concentration, nucleation etc.

Discerning the oxygen defects

Effective control and design of oxygen vacancy sites within the material are crucial for intended applications. There are some indirect indications for the presence of oxygen vacancies (Vo^i or Vo^{ii}) in our synthesized materials (MO_{w60}, MO_{w90}, MO_{ipa90}), as evidenced by spectroscopic characterizations. FT-IR spectra (Fig. 1) showed some peaks, due to single oxygen atom interaction with three molybdenum atoms (548 cm^{-1}), Mo–O–Mo bonding with stretching vibrations of O_3 atoms (864 cm^{-1}), Mo–O vibrations (601 cm^{-1}), and Mo_2–O_4 bonding by solvolyzing H_2O molecules (466 cm^{-1}). Similarly, Raman spectra of the samples also showed peaks for O–Mo–O bonds (300–700 cm^{-1}) and Mo–O–Mo bonding (700–1000 cm^{-1}). But again, these are all qualitative indications only.

Oxygen vacancies (Vo^i, Vo^{ii}), which alter the electronic environment at molecular level, is detectable, by observing changes in the binding energies of Mo-3d and O-1s peaks in XPS spectra too. Reduced oxidation states of Mo (from Mo^{6+} to Mo^{5+} or Mo^{4+}) undergo shift in Mo-3d peaks, while the O-1s peaks undergo shift and change in shape as described in XPS data interpretation (Fig. 9, Table S5). However, quantitative analysis of these oxygen peaks only could reveal the concentration and distribution of oxygen vacancies, which is crucial for the interpretation of mechanism of phase transition.

Hence, we have quantified the area under the O-1s peak for all 3 samples (Fig. 9b, Table S5), which conveys that the thermodynamically most stable α-MoO_3 obtained via w90 treatment possess more oxygen concentration than the metastable h-MoO_3 obtained from w60, and h and α-MoO_3 from ipa90 treatments. Table S5 shows that more the oxygen content, better the stability and phase transition. Because, the oxygen deficient and defective $(MoO_{3-(x+y)})^{n+}$cation is hungry of oxygen atoms which has to be quenched by supplying fresh oxygen atoms and then be stabilized by protons, coming from either reagents or solvents. These results suggest that w90 treatment (solvolysis) could have efficiently refilled the oxygen vacancies in $(MoO_{3-(x+y)})^{n+}$, by the incoming oxygen atoms from H_2O solvent and protonation of MoO_4^{2-} intermediate by the same H_2O, with the complete phase transition ($am \rightarrow h \rightarrow \alpha$-$MoO_3$). Whereas in w60, ipa90 treatments (solvolysis), the substitution of oxygen atoms from solvents: H_2O at 60 °C, iso-propanol at 90 °C, was not that efficient, to fill the oxygen vacancies and for the

protonated stabilization of MoO_4^{2-} intermediate. Hence, they were left with incomplete and partial transitions like, only up to h-MoO_3 and mixed h and α-MoO_3 respectively. So, it was purely because of elevated temperature (90 °C) and more protic solvent like H_2O, the phase transition propelled from h- to α-crystalline structure. Thus, from XPS data perspective, it was inferred that MO_{w60}, MO_{ipa90} samples possess more oxygen vacancies than MO_{w90}, in which the vacancies were efficiently refilled.

The real limitation here is that the identification of source of oxygen atoms in α-MoO_3 and h-MoO_3 product phases. For this, we need an in-depth spectroscopic (Mass/IR) study of O^{18} isotope labelled-H_2O^{18} mediated VST of MoO_{3-x}. Another way of characterizing the oxygen vacancies would be using in-situ EPR spectroscopy to find out the nature of oxygen defected and then refilled. This way the exact nature and distribution of oxygen vacancies can be characterized. We keep this task for our future work and would definitely want to report the scientific community later.

Further, our strategy to control the oxygen defects was an indirect approach by measuring band gaps via UV–Vis spectroscopy. The principle is that introducing oxygen vacancies creates new energy levels and when their concentration exceeds 0.1%, significantly alters the energy bands in the material. In transition metal oxide semiconductors, oxygen vacancies modify the valence band, which consists mainly of the oxygen 2p orbital, that leads to changes in the material's optical absorption properties[47]. Yuan et al. studied how different calcination rates for metal oxides influence the number of oxygen vacancy sites. Their findings suggest that increasing oxygen vacancies can reduce the band gap value of the material[48].

In our case, Fig. 3b, showcases the determination of band gaps (E_g) through Tauc plot analysis using the UV–vis spectrum. The calculated E_g values for MO_{w60} (h-MoO_3), MO_{w90} (α-MoO_3), and MO_{ipa90} (h and α-MoO_3) were 2.94 eV, 2.45 eV, and 1.51 eV respectively. Based on above mentioned Yuan et al's postulate, the total oxygen vacancies (Vo = Vo^i + Vo^{ii}) in our samples could be in the order for; MO_{ipa90} > MO_{w90} > MO_{w60}. This indicated that organic solvent like *iso*-propanol (ipa90) medium could have created more secondary oxygen vacancies (Vo^{ii}) than an aqueous solvent (H_2O) medium (w90), followed by w60 medium, during VST. However, the solvolysis efficiency of refilling oxygen in the vacancy sites followed by proton mediated stabilization of MoO_4^{2-} intermediate was better at 90 °C, especially with H_2O. Hence the degree of phase transition to α- phase, in our samples, was in the reverse order for; MO_{w90} > MO_{ipa90} > MO_{w60}. At 60 °C in H_2O, both the Vo created as well as the solvolysis were less and inefficient. Thus, MO_{w60} ended up with phase transition ($am \rightarrow h$) only up to metastable hexagonal phase (h), whereas MO_{w90} resulted in complete phase transition from am- to h-, then to α-MoO_3, and finally MO_{ipa90} yielding only partial transition (mixed phases of h and α-MoO_3). Here comes a disagreement between, XPS and UV–Vis data for MO_{w60} sample, in which O-1s area suggested the presence of more Vo, whereas E_g value indicated less Vo in it. It may be because of the less expression of oxygen atoms from the meta stable h-MoO_3 (MO_{w60}) in XPS causing less sensitivity towards oxygen atoms. We will sort out this discrepancy in our future work.

Thus, oxygen defects can be correlated to bang gaps (E_g) and vice-versa via UV–Vis spectroscopy. Therefore, the E_g values are of one kind of indirect indication for us, to change the synthesis parameters and have a control over the distribution and concentration of oxygen defects within the crystal lattice. This was our strategy to control the oxygen vacancies in quantitative terms.

Others in reported methods, often employed high temperature annealing treatment in a reducing atmosphere to generate oxygen vacancies in metal oxide materials. The concentration of these vacancies can be controlled to some extent by adjusting parameters such as temperature, vacuum level, atmosphere composition, inert gas and other process variables. But we have controlled it through simple vacuum assisted solvolysis technique (VST) in a cost-effective way, in our present study. Thus, we believed that applying a controlled heat under vacuum and then neutralizing the positively charged defective MoO_3 using protic solvents, could yield desired crystalline phase transition in our materials. This was the hypothesis behind our experimental planning and execution.

Repeatability and reproducibility of *DEST* method for an eco-friendly, energy efficient, low temperature phase transition in MoO₃

Wet-chemical syntheses would often result in issues like reproducibility and heterogeneity in the sample. We have carefully avoided these issues as much as possible, by paying more attention on exact repetition of operation parameters (precursor weight, temperature, time, vacuum level, solvent quantities) in multiple synthesis trials to confirm the repeatability and reproducibility (Fig. S3). SEM (Fig. 7a–c) showed the homogeneity within each sample in terms of particle size and morphological appearance.

Currently we rely on the microscopic techniques and XRD to address sample heterogeneity if anything of that sort found. For e.g. The Rietveld analysis of the X-ray diffraction pattern of MO_{ipa90} confirms the presence of (010) of h-MoO_3 and #(020) of α-MoO_3 phases, within the same sample (Fig. 4c). This indicates the heterogeneity and composition of mixed phases, but predominately composed of h-MoO_3. The software reveals that the mixed phase contains 72.6% of h-MoO_3 and 27.4% of α-MoO_3. This ratio can be controlled by tuning the solvent amount, mixtures of solvents, ratios of solvents, material concentration etc. It is good to maintain the homogeneity and avoid heterogeneity in the samples prepared. But sometimes heterogeneity could also give us unexpected positive turn around in applications, due to synergy between multiple phases. So, it is not always undesirable to have heterogeneity in the synthesized samples.

Figure 4 and Fig. S3 show the XRD spectra of samples from original batch (Batch 1) and reproduced materials (Batch 2) respectively. Table S6 shows the comparison of X-Ray diffraction angles (2θ) between two batches of samples. The results suggest that careful repetition of synthesis parameters (temperature, time, vacuum level, solvent volume, precursor amount) yielded same materials as the 2θ values were almost similar, except few fractions of degree deviation, here and there. Hence, this *DEST* synthesis protocol is reproducible. Thus, we believe that our experimental design is reliable and has clear control over all the variables involved in the products' formation.

Discrepancies between our findings and reported results

Tables S7, S8 show how our method of executing phase transition in MoO_3 differs from other previously reported methods. Basically, our method doesn't require very high temperature for phase transition and also employs facile procedure with eco-friendly low boiling solvents, as against the phase transitions which are often carried out at high temperatures (150–450 °C), that consumes lot of thermal energy and energy costs.

It is widely reported that amorphous (non-crystalline/nano) materials are always good starting points for the formation of phase-pure materials of specific mono-morph, through controlled crystallization[49]. Our work involves in converting amorphous MoO_{3-x} into h-MoO_3, α-MoO_3 and mixed phases (h and α) at the maximum 60–90 °C using either water or *iso*-propanol in a simple vacuum distillation unit. However, the reported methods start with crystalline precursor materials like NH_4^+, Na^+ cation containing molybdate, heptamolybdate compounds. These cations play a catalytic/promotor role in nucleation and crystal growth steps of various forms of MoO_3, which is not the case in our method. Other major difference is that they use non-eco-friendly, stochiometric reagents like highly corrosive, strong mineral acids e.g., HCl, HNO_3 etc., in order to hydrolyze molybdate and heptamolybdate feed molecules, during hydrothermal syntheses. They also report that variety of crystalline phases can be formed at different temperatures and various ratios of precursor to acid solvent. But some of their lattice parameters[21,35] and band gaps have notable changes from our values, for the given crystal structure. This comparative preparation and phase transition conditions for MoO_3 declares that our method is better than the reported methods. Thus, we defend our work, as a reasonable contribution to nanomaterials synthesis field.

The discrepancies between our method and reported methods can throw up new application possibilities in electrochemistry, energy storage, photocatalysis, solar cells, adsorbents, etc., as every method produce a material with unique properties such as lattice parameters, band gap, interlayer spacing etc. This also has lot of scope for extensive characterization of these materials which can impact overall trajectory of materials science research.

Electrochemical investigations of *DEST*-made MoO$_3$ polymorph 2D nanosheet materials

Any material in the universe should justify its existence for an application. Hence, we have investigated the synthesized materials for supercapacitor performance, which is our model application study. Though it is proclaimed that α-MoO_3 is the most electroactive phase, still we wanted to have a comparison with h-MoO_3 and mixed phase (h and α-MoO_3), as they were prepared from new synthetic route. We never know what are all happening behind in an unknown synthesis method. So, it is good to make an attempt and see the results to have better confirmation.

The electrochemical performance of *DEST*-made MoO_3 polymorphs modified glassy carbon electrodes (GCE) were examined by cyclic voltammetry (CV), galvanostatic charge–discharge (GCD) and electrochemical impedance spectroscopy (EIS) measurements. There was no leaching of loaded material from GCE surface observed, in entirety of experiments. The area under the curve in CV (Fig. 10a) for α-MoO_3 (MO_{w90}) was significantly greater than that of other polymorphs; h-MoO_3 and mixed h and α-MoO_3 (MO_{w60}, MO_{ipa90}) at the scan rate of 20 mV s^{-1}, showing significantly increased charge/power density. Figure 10b, showing the CV curves exclusively for the best performing α-MoO_3 (MO_{w90}), recorded in the potential range, -1.0 to 0 V and at different scan rates starting from 20 to 100 mV/s. The area under the curve increased when the scan rate increased and all CV curves exhibited quasi-rectangular shapes without any redox peaks, indicating the electrochemical stability of the material.

Further, galvanostatic charge–discharge curves (GCD) were recorded at current density, 0.125 A/g, to assess the capacitance behavior of MoO_3 polymorphs, h-MoO_3 (MO_{w60}), α-MoO_3 (MO_{w90}) and h and α-MoO_3 (MO_{ipa90}), as shown Fig. 10c. All three MoO_3 polymorphs were displaying a non-linear charge–discharge curve, demonstrating their pseudocapacitive nature. As expected, α-MoO_3 (MO_{w90}) showed slow and steady pace of charging and discharging, effectively suggesting the superior capacitance behavior than that of other polymorphs (based on the Eq. 1 in 'Methods' section). GCD measurements were also done at different current densities for the best performing α-MoO_3 (MO_{w90}) as shown in Fig. 10d. Current densities higher than 0.125 A/g was found to be detrimental in terms of capacitance measurement, thus suggesting 0.125 A/g was the optimum current density for the *DEST*-made MoO_3 polymorphs.

Electrochemical impedance spectroscopy (EIS) experiment was conducted in order to learn more about the electrocapacitive behavior of the aforementioned MoO_3 polymorphs. Figure 10e displays the Nyquist plot for each sample. All three samples showed a no electrode resistance, but electrolyte resistance. The impedance response in the Nyquist plot can be split into two regions, (i) an initial semi-circular electrolyte resistance region, and further (ii) an upward straight line of resistance free region. The semicircle directly indicates the initial resistance that the material experiences, which is in the order for h-MoO_3 (MO_{w60}) > h and α-MoO_3 (MO_{ipa90}) > α-MoO_3 (MO_{w90}). Thus, confirming the superior conducting and capacitive nature of α-MoO_3 (MO_{w90}) over other polymorphs.

Figure 10f shows the calculated specific capacitance values at different scan rates for all three MoO_3 polymorphs. Based on the calculations using Eq. (1) and Fig. 10f, the specific capacitance for MO_{w60} (h-MoO_3), MO_{w90} (α-MoO_3) and MO_{ipa90} (h and α-MoO_3) were found to be 14.3 Fg^{-1}, 256 Fg^{-1}, 41.8 Fg^{-1} respectively. Thus, MO_{w90} (α-MoO_3) proved to be having 18 times better capacitance than its sister material MO_{w60} (h-MoO_3) and 6 times better performing than its counterpart MO_{ipa90} (h and α-MoO_3). This result is at par excellence than other reported materials in the literature. The comparative performance analysis with existing α-MoO_3 and non-MoO_3 coated electrode materials in literature, is furnished in Tables S9, S10. Similar to earlier mentioned discrepancies in lattice parameters and band gaps, based on preparation method and phase transition temperature (Tables S7, S8), the reported capacitance values for α-MoO_3 also differs from our value (256 Fg^{-1}), but largely in decrement. It shows that the reported α-MoO_3 materials, where the phase transition was achieved only above 400 °C, exhibit specific capacitance, only below 200 Fg^{-1}. The electrode materials other than MoO_3 (non-MoO_3) also show similar trend i.e., < 200 Fg^{-1}. Thus, our material is competitive and promising, comparatively with other reported MoO_3 materials and conducting polymers.
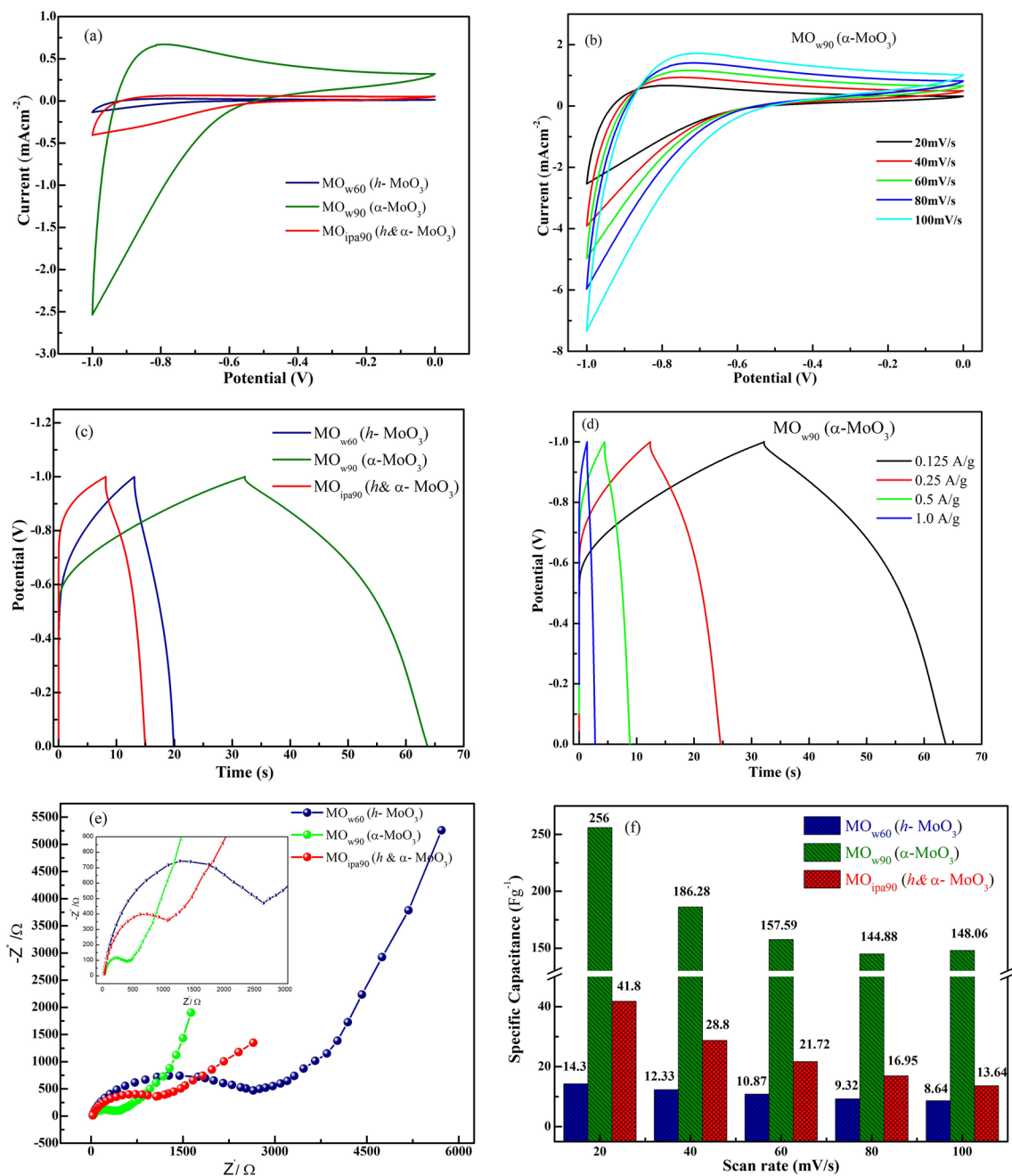
Figure 10. Electrochemical performances of *DEST*-made MoO$_3$ polymorphs modified glassy carbon electrodes (GCE): (**a**) Cyclic Voltammetric (CV) curves for all polymorphs at the scan rate of 20 mV s^{-1}, (**b**) CVs at different scan rates for α-MoO$_3$ (MO$_{w90}$), (**c**) Galvanostatic Charging-Discharging (GCD) characterization for all polymorphs at the current density of 0.125 A/g, (**d**) GCD profiles at different current densities for α-MoO$_3$ (MO$_{w90}$), (**e**) Electrochemical impedance spectroscopy (EIS) for all polymorphs, (**f**) Specific capacitance values of all polymorphs at different scan rate.

Structure–activity relationship

Role of oxygen defects

Oxygen vacancies (Vo), which are the predominant point defects in metal oxides, have the tendency to increase the electron density in the local environment of the molecular structure. This increase is caused by electrons donated by the escaped oxygen atoms, leading to an improved electrical conductivity and catalytic performance of the product material. e.g., particularly in n-type MoO_3 semiconductors[50]. Oxygen vacancies (Vo) can also significantly increase the interlayer spacing because of loss of oxygen atoms. This also enhances the electrochemical activity and thereby promoting faster charge storage kinetics[51]. For example, annealing in a reducing environment can increase oxygen vacancy concentration, improving lithium–ion intercalation kinetics in battery applications. Thus, the control over oxygen defect formation can result in desired electrochemical properties such as conductivity, capacitance etc. in the target material. In our case, MO_{ipa90} (h and α-MoO_3) sample has more oxygen vacancies (Vo) than MO_{w90} (α-MoO_3) sample, based on the E_g values for MO_{w60} (h-MoO_3), MO_{w90} (α-MoO_3), and MO_{ipa90} (h and α-MoO_3) ; 2.94 eV, 2.45 eV, and 1.51 eV respectively (Vo: $MO_{ipa90} > MO_{w90} > MO_{w60}$). However, the electro-capacitance activity was higher (256 Fg^{-1}) with MO_{w90} sample than MO_{ipa90} sample (41.8 Fg^{-1}). Hence, this suggests that more than oxygen vacancies, the lattice parameters in the crystalline phase and interlayer spacing were playing a major role in electrochemical responses of the MoO_3 polymorphs.

Role of crystal characteristics

Characteristics like lattice parameters, density of states, surface area, and morphology vary for different crystal structures of the same compound. Lattice parameters influence ion intercalation and diffusion pathways, whereas the density of states near the Fermi level impacts electronic conductivity and charge storage. Surface and morphological features like area, roughness and defects affect the availability of catalytic active sites for charge storage. Hence, the overall crystal structure influences electrochemical properties consequently, in large.

MoO_3 exists in polymorphs, such as h-MoO_3 (hexagonal), α-MoO_3 (orthorhombic), β-MoO_3 (monoclinic), and γ-MoO_3 (cubic)[4–7]. The structure of different phases of MoO_3 is established by how the foundational octahedral unit (MoO_6) shares its corners and edges for ions' interactions[10]. The configuration of MoO_6 octahedrons (Fig. 11a) is influenced by external factors including temperature, pressure, and impurities[52]. The β-MoO_3 structure (Fig. 5b) is made up of MoO_6 octahedra that share corners in three dimensions and thus creating a monoclinic structure. It is similar to the structure of WO_3 and related to distorted ReO_3 type structure, thus classified as an empty A-site perovskite (ABO_3). β-MoO_3 holds only corner sharing oxygen atoms, whereas h-MoO_3 and α-MoO_3 having both corner and edge sharing oxygen atoms. The h-MoO_3 is constructed by zigzag chains of same MoO_6 octahedra (Fig. 11b,c), along [001] direction, which creates massive 1D tunnels. These chains are interlinked between them at *cis*-position. Whereas, α-MoO_3 is composed with edge-sharing zigzag rows and corner-sharing rows of deformed MoO_6 octahedra along the [001] and [100] directions respectively, to form a planar double layer (2D), giving rise to an anisotropic structure. Strong covalent and ionic bonds dominate the internal interactions in the deformed MoO_6 octahedra, which are kept together in the vertical [010] direction by weak van der Waals' forces, that causes the stratification in α-MoO_3. Double layers of MoO_6 octahedra are arranged in a (ABA) pattern and repeated in the *ab* plane along the *b* axis to produce a layered framework in the
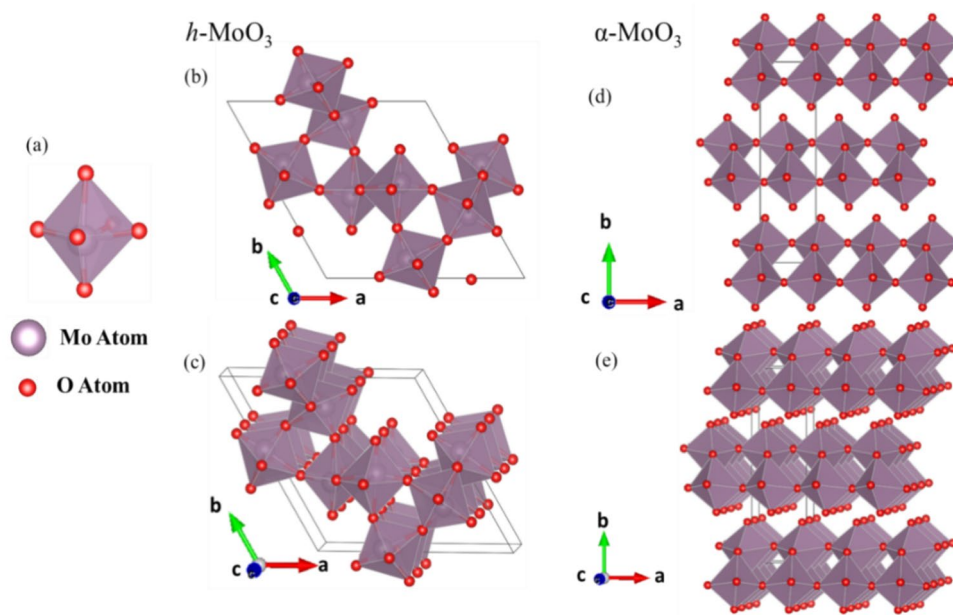

Figure 11. A schematic presentation of MoO_6 octahedron (**a**), composed of Mo and O atoms, forming MoO_3 crystal structures; h-MoO_3 (**b,c**), α-MoO_3 (**d,e**). The unit cell dimensions are denoted by the grey lines.

crystal structure of α-MoO₃[9,26] (Fig. 11d,e). These structural differences between various crystalline phases can have influence over the electrochemical properties of MoO₃ polymorphs.

Among the MoO₃ polymorphs, α-MoO₃ generally provides the highest specific capacitance due to its thermodynamic stability and favorable layered structure that facilitates ion intercalation and de-intercalation[11,15]. However, the actual performance can also be influenced by other factors such as synthesis methods, morphology, particle size, thickness of the nanosheets, lattice parameters, interlayer spacing etc. In our case (Table 1), the α-MoO₃ (MO$_{w90}$) possess smaller lattice parameters (a = 3.95, b = 3.95, c = 3.72) than h-MoO₃ (a = 10.61, b = 10.61, c = 3.72), and an enhanced interlayer spacing of 3.8 Å (101). This could have resulted more surface area in α- MoO₃, than h-MoO₃ (MO$_{w60}$), as α-MoO₃ was derived from the intermediate (MoO$_{3-(x+y)}$)$^{n+}$ having more secondary oxygen vacancies (Vo^{ii}), caused by w90 treatment in VST. It is also believed that orthorhombic (α-) structure possess high fraction of surface exposed atoms[53,54] than hexagonal structure (h-), due to smaller lattice and enhanced interlayer spacing. Hence it could have more active sites for charge storage. Thus, these structural differences between the metastable h-MoO₃ and thermodynamically stable α-MoO₃ have their direct influence on the capacitance values; former perfoms (14.3 Fg⁻¹) poorer than latter (256 Fg⁻¹), whereas the mixed phase, performs moderately (41.8 Fg⁻¹).

We were expecting a synergistic effect from the mixed-phase MoO₃ (h and α) viz-a-viz its electrochemical performance. But the result did not meet our expectation. The mixed phase usually causes variations in the local chemical environment, including differences in stoichiometry, surface defects, oxidation states, adsorbed species, and bonding configurations. These variations affect the electron density around Mo atoms. We also believe that there might be some unknown interfacial sites which could have distorted lattice parameters and modified density of states near the Fermi level. These interfaces at the phase boundaries can influence ion diffusion pathways and charge transfer, which will have an overall impact on electronic conductivity, charging-discharging ability of the material. To experimentally prove this interfacial phenomenon, pure h-MoO₃ and pure α-MoO₃ crystalline phases can be physically mixed in various known ratios and then be characterized by UV–Vis, XRD, XPS, CV, GCD. This might offer a preliminary understanding of how the bulk level-interface influence the electrochemical behaviour of the mixed phase. Based on this, MoO₃ polymorphs materials possesing lattice level-interfaces can be synthesized and further scrutinized by Rietveld refinement technique in XRD using FULLPROF program.

These new lattice level-interfaces can be created by tuning the synthesis parameters especially the solvents. We realize that the current ratio (72.6% of h-MoO₃ and 27.4% of α-MoO₃) in the mixed phase was not favorable for enhanced capacitance. Hence, for e.g. a synthesis of (50:50) of h-MoO₃: α-MoO₃ or a more of α-MoO₃ and less of h-MoO₃ combination (75:25, 60:40), could help in achieving the desired results, as we already know that α-MoO₃ is relatively more electro-active and capacitive. We believe that this ratio can be adjusted by employing different organic solvents (ethanol, acetic acid etc.) for the creation of defective (MoO$_{3-(x+y)}$)$^{n+}$ and its subsequent hydrolysis with different degrees of phase transition. This way a final product of lattice level-mixture of various ratios of MoO₃ polymorphs can be obtained. This study could enable the most anticipated synergistic effect from the mixed-phase MoO₃ (h and α) for its enhanced electrochemical performance.

One interesting point to be noted here is that, even though the interlayer spacing in mixed-phase MoO₃ (h and α) was lower (2.5 Å) than h-MoO₃ (MO$_{w60}$) (3.47 Å) (Table 1), it was more electro-active than h-MoO₃. So, there is definitely a scope for enhancing its capacitance further through synergistic effect, given right preparation conditions are used. We keep this more nuanced work for our future activities.

Factors affecting electrochemical behavior

Based on the results and literature evidences, the factors which might largely affect the electrochemical behavior of MoO₃ are (a) synthesis methods, (b) oxygen vacancies, (c) crystal structure and interfaces, (d) morphology, (e) particle size, (f) thickness of the nanosheets, (g) interlayer spacing etc. However, the actual performance can also be influenced by factors other than these material properties; for e.g., specific conditions of electrochemical testing such as (a) amount of material loading on GCE, (b) choice of electrolyte, (c) electrodes' configuration

Structure–activity relationship (SAR)		XRD			HRTEM		UV–Vis	XPS	CV
		Lattice parameters							Specific capacitance C_p F/g
S. no.	Sample ID	a	b	c	Interplanar spacing (d) Å		Band gap (E_g)	O-1s peak area (×10⁴)	
1	MO$_{w60}$ (h-MoO₃)	10.61	10.61	3.72	(011)	3.47	2.94	20.93	14.3
					(120)	3.40			
					(030)	3.05			
2	MO$_{w90}$ (α-MoO₃)	3.95	3.95	3.72	(210)	3.2	2.45	42.76	256
					(101)	3.8			
3	MO$_{ipa90}$ (Mixed Phases of 72.6% h-MoO₃ and 27.4% α-MoO₃)	10.61/3.98	10.61/13.86	3.72/3.71	(501)	2.2	1.5	24.92	41.8
					(121)	2.5			

Table 1. Comparison of crucial characterization data of MoO₃ polymorphs to discern their electrochemical activity.

etc. Optimizing all these factors can enhance the specific capacitance of each mono-morph to the desired performance level. We will look into these details very elaborately in our future work.

Future prospects

Apart from the proposed future courses of actions mentioned in the discussion part, we would also like to scale up of the production of MoO_3 and studying its long-term stability through longer hours experiments (charging-discharging), performing multiple cycles of GCD. We are excited to report our findings in our next communication.

Conclusion

In summary, physical vapor deposited (PV**D**) amorphous MoO_{3-x} nano powder was meticulously extracted by ultrasonication (US**E**) in strategically chosen green solvents. Further, the extracted MoO_{3-x} nanomaterials were recrystallized by an eco-friendly, energy efficient, vacuum assisted solvothermal (VS**T**) approach at very low temperature in water or *iso*-propanol. The combination of operating parameters in this *DEST* synthesis has truly yielded h-MoO_3 even at 60 °C and a fascinating phase transition from h-MoO_3 to α-MoO_3 at very low temperature *ca.* 90 °C, in just water. On the other hand, *iso*-propanol as a solvent, produced mixed phases (h and α) of MoO_3 at 90 °C. The different phases of synthesized MoO_3 were identified and confirmed by an extensive XRD spectroscopic scrutiny and other characterizations. We believe that the implantation of oxygen defects followed by its solvolysis with the protic nature of the solvent and optimally very low temperature selection, resulted in an efficient proton mediated phase transition ($am \rightarrow h \rightarrow \alpha$-$MoO_3$) in first-of-its kind. Because, other reported methods have always used very high calcination temperature ranges (300–1500 °C) to achieve this phase transition in MoO_3.

To utilize the synthesized 2D nanosheets of MoO_3 polymorph materials in real world application, a series of electrochemical investigations have been carried out under CV, GCD conditions. MO_{w90} (α-MoO_3) found to be exhibiting 18 times better specific capacitance performance than MO_{w60} (h-MoO_3) and six fold better activity than MO_{ipa90} (h and α-MoO_3). We reasoned out that, α-MoO_3 (MO_{w90}) possess smaller lattice parameters and an enhanced interlayer spacing, which could have resulted more surface area and high fraction of surface exposed atoms in it, than h-MoO_3 (MO_{w60}), leading to more active sites for charge storage. These results convey the message that, by finetuning the synthesis parameters, electrochemical conditions further, *DEST* produced α-MoO_3 2D nanosheets can be made as the most promising upcoming candidates for creating next generation high-performance supercapacitors.

Experimental

Materials

Molybdenum Trioxide Extra Pure (MoO_3) and *iso*-propanol (($CH_3)_2CHOH$) were purchased from Loba Chemie. For the physical vapor deposition of MoO_3 precursor the thermal evaporation BC 300 box coater was used. Milli-Q water was used in entire experiment.

Methods

Preparation of molybdenum trioxide (MoO_{3-x}) thin film by physical vapor deposition (PVD)

Physical vapor deposition (PVD) of commercially acquired MoO_3 powder (bulk material) was performed by using a less-expensive, homemade thermal box coater equipment. The glass substrates were cleaned before use, through Radio Corporation of America (RCA) procedure to remove organic and inorganic impurities settled on it[55], followed by UV treatment to make the substrate's surface hydrophilic[56,57]. Then the target material, molybdenum trioxide powder was taken and placed on the molybdenum boat in the thermal-ultrahigh vacuum evaporation set-up. MoO_3 powder was evaporated at 700 °C and slowly deposited as thin films, layer by layer on the cleaned glass substrates, under the chamber pressure of 10^{-7} Pa. The thickness of the MoO_3 films were controlled to be 150 nm by real time quartz crystal thickness monitor with constant rate of deposition ca. 0.3 nm/s[58,59]. Thus, the thin films of amorphous MoO_{3-x} materials were achieved (Fig. S4).

Collection of amorphous MoO_{3-x} by ultrasonic extraction (USE)

The extraction of PVD-made MoO_{3-x} thin films was carried out using lab ultrasonic bath (USE). The MoO_{3-x} thin film coated glass substrates were immersed in two different polar solvents; water (H_2O) and *iso*-propanol (($CH_3)_2CHOH$), separately, to disperse the amorphous MoO_{3-x} flakes in respective solvents, by the application of sonication treatment for one hour. Thus, MoO_{3-x} thin films were peeled off carefully from the glass substrates in the form of nano powder and dissolved in above mentioned polar solvents. This led to get two transparent, homogeneous MoO_{3-x} solutions, separately (Fig. S4).

Recrystallization of MoO_{3-x} by vacuum assisted solvothermal treatment (VST)

Further, the above aqueous and alcoholic MoO_{3-x} solutions were subjected to vacuum assisted solvothermal treatments (VST) using lab rotavapor equipment. The rotary evaporator set up basically had MoO_{3-x} solution containing rotating round bottom (RB) flask heated by metallic water bath filled with Milli-Q water and a chiller unit maintained at 7 °C to condense the extracted solvent. The aqueous and alcoholic MoO_{3-x} solutions were heated at different temperatures (60, 90 °C and 90 °C respectively) under constant 120 mbar vacuum, with the rotation speed of 175 rpm. The process was run continuously until entire solvent got evaporated with the outcome of MoO_{3-x} recrystallization (Fig. S4). At the end, three different colors of MoO_3 (greyish green, blue and black) wet flakes were obtained for the respective treatments. These flakes were further vacuum dried in an oven at 60 °C to obtain the rigid solid flakes of (h-), (α-), (h and α-) MoO_3 materials, correspondingly.

We have marked the *DEST*-made MoO_3 samples as MO_{w60} (recrystallized from water at 60 °C), MO_{w90} (recrystallized from water at 90 °C) and MO_{ipa90} (recrystallized from *iso*-propanol at 90 °C).

Characterization

Fourier Transform Infra-Red (FT-IR) Spectroscopy analyses of *DEST*-made MoO_3 crystalline samples were carried out by Shimadzu Affinity S2, using KBr pellet method, in the wavenumber range of 500–4000 cm^{-1}. Confocal Raman Spectroscopy of the samples was carried out by using WiTec Alpha 300 Germany equipment. Ultraviolet (UV)–Visible spectra of samples were recorded using Jasco V-770 Spectrophotometer. X-Ray Diffraction (XRD) patterns of samples were collected using PANalytical X-Ray Diffractometer, in the range of $2\theta = 10°$ to 80°. The XRD patterns were simulated using the PCW software, utilizing crystallographic parameters such as space group, lattice parameters, and atomic positions from the literature. High Resolution Transmission Electron Microscopic (HRTEM) analysis was carried out using JEOL JEM 2100 microscope. Scanning electron microscopy (SEM) was performed by using Carl ZEISS EVO 18-Germany equipment with AMETEK Team V.4.3 EDS detector. Atomic Force Microscopy (AFM) was carried out using CS Instrument of Model No: S-SPM-00001. X-ray photoelectron spectra (XPS) were performed using K ALPHA + Thermo Fisher Scientific Instrument.

Electrochemical characterizations of all samples were carried out by M/S Biologic Science electrochemical workstation with a standard three-electrode cell configuration. The reference electrode was a standard Ag/AgCl, the counter electrode was Pt wire, and the working electrode was glassy carbon electrode (GCE). Initially, 2 mg of 2D MoO_3 was dispersed in 500 µl of a polar solvent. Subsequently, 5 µl of this dispersion was applied on the GCE, by drop-casting technique, to modify its surface and as a fabrication of supercapacitor. An aqueous solution of 1 M Na_2SO_4 was used as the electrolyte, throughout the experiments. The electrochemical performance of different MoO_3 polymorphs materials and the supercapacitor application was evaluated using cyclic voltammetry (CV) and galvanostatic charge–discharge method (GCD) respectively.

Equation (1) was used to calculate the specific capacitance from CV curves.

$$specific\ capacitance = Cs = \frac{\int i\ dV}{2m\ \Delta V \times scan\ rate} \tag{1}$$

Cs: specific capacitance, idV: integral part that represents the area below the cyclic voltammetry curve, m: mass of drop casted electrode material, ΔV: potential window.

Data availability

The data that support the findings of this study are available from the corresponding author upon request.

References

1. Liang, R. *et al.* Transition metal oxide electrode materials for supercapacitors: A review of recent developments. *Nanomaterials* **11**, 1248 (2021).
2. Wan, Y. *et al.* Oxygen-deficient metal oxides for supercapacitive energy storage: From theoretical calculation to structural regulation and utilization. *Adv. Energy Sustain. Res.* **3**, 2100221 (2022).
3. Kalantar-Zadeh, K. *et al.* Synthesis of nanometre-thick MoO_3 sheets. *Nanoscale* **2**, 429–433 (2010).
4. Muthamizh, S., Sengottaiyan, C., Jayavel, R. & Narayanan, V. Facile synthesis of phase tunable MoO_3 nanostructures and their electrochemical sensing properties. *J. Nanosci. Nanotechnol.* **20**, 2823–2831 (2020).
5. Ren, H., Sun, S., Cui, J. & Li, X. Synthesis, functional modifications, and diversified applications of molybdenum oxides micro-/nanocrystals: A review. *Crystal Growth Des.* **18**, 6326–6369 (2018).
6. Etman, A. S. *et al.* Facile water-based strategy for synthesizing MoO_{3-x} nanosheets: Efficient visible light photocatalysts for dye degradation. *ACS Omega* **3**, 2193–2201 (2018).
7. Paraguay-Delgado, F. *et al.* h-MoO_3 phase transformation by four thermal analysis techniques. *J. Therm. Anal. Calorim.* **140**, 735–741 (2020).
8. Chen, X., de Boer, R. M., Kosari, A., van Gog, H. & van Huis, M. A. Thermal reduction of MoO_3 particles and formation of MoO_2 nanosheets monitored by in situ transmission electron microscopy. *J. Phys. Chem. C* **127**, 21387–21398 (2023).
9. De Castro, I. A. *et al.* Molybdenum oxides—From fundamentals to functionality. *Adv. Mater.* **29**, 1701619 (2017).
10. Zheng, L., Xu, Y., Jin, D. & Xie, Y. Novel metastable hexagonal MoO_3 nanobelts: Synthesis, photochromic, and electrochromic properties. *Chem. Mater.* **21**, 5681–5690 (2009).
11. Sharma, R., Sharma, A. K., Jha, R. & Sarkar, A. Stable α-MoO_3 nanocrystals and its doped variants with unique morphologies under optimized reaction conditions for efficient electrochemical and photochromic performances. *Mater. Chem. Phys.* **280**, 125813 (2022).
12. Nadkarni, G. S. & Simmons, J. G. Electrical properties of evaporated molybdenum oxide films. *J. Appl. Phys.* **41**, 545–551 (1970).
13. Sabhapathi, V. K. *et al.* Optical absorption studies in molybdenum trioxide thin films. *Phys. Status Solidi (A)* **148**, 167–173 (1995).
14. Ali, H. M., Shokr, E. K., Elkot, S. A. & Mohamed, W. S. Promising molybdenum trioxide films for optically detectable gas sensor and solar cell applications. *Mater. Res. Express* **6**, 126451 (2020).
15. An, C., Zhang, Y., Guo, H. & Wang, Y. Metal oxide-based supercapacitors: Progress and prospectives. *Nanoscale Adv.* **1**, 4644–4658 (2019).
16. Jafari, A., Anarjan, N. & Jafarizadeh-Malmiri, H. Effects of rotation speed and time, as solvent removal parameters, on the physico-chemical properties of prepared α-tocopherol nanoemulsions using solvent-displacement technique. *Food Sci. Biotechnol.* **29**, 371–378 (2020).
17. Jadkar, V. *et al.* Synthesis of orthorhombic-molybdenum trioxide (α-MoO_3) thin films by hot wire-CVD and investigations of its humidity sensing properties. *J. Mater. Sci. Mater. Electron.* **28**, 15790–15796 (2017).
18. Han, Y., Rheem, Y., Lee, K.-H., Kim, H. & Myung, N. V. Synthesis and characterization of orthorhombic-MoO_3 nanofibers with controlled morphology and diameter. *J. Ind. Eng. Chem.* **62**, 231–238 (2018).
19. Chiang, T. H. & Yeh, H. C. A novel synthesis of α-MoO_3 nanobelts and the characterization. *J. Alloys Compd.* **585**, 535–541 (2014).

20. Song, J., Ni, X., Gao, L. & Zheng, H. Synthesis of metastable h-MoO$_3$ by simple chemical precipitation. *Mater. Chem. Phys.* **102**, 245–248 (2007).
21. Chithambararaj, A. & Bose, A. C. Hydrothermal synthesis of hexagonal and orthorhombic MoO$_3$ nanoparticles. *J. Alloys Compd.* **509**, 8105–8110 (2011).
22. Du, L. *et al.* Synthesis of a novel amphoteric copolymer and its application as a dispersant for coal water slurry preparation. *R. Soc. Open Sci.* **8**, 201480 (2021).
23. Sen, S. K. *et al.* An investigation of 60 Co gamma radiation-induced effects on the properties of nanostructured α-MoO$_3$ for the application in optoelectronic and photonic devices. *Opt. Quantum Electron.* **51**, 1–15 (2019).
24. Kothaplamoottil Sivan, S. *et al.* Greener assembling of MoO$_3$ nanoparticles supported on gum arabic: Cytotoxic effects and catalytic efficacy towards reduction of p-nitrophenol. *Clean Technol. Environ. Policy* **21**, 1549–1561 (2019).
25. Varghese, J., Siponkoski, T., Nelo, M., Sebastian, M. T. & Jantunen, H. Microwave dielectric properties of low-temperature sinterable α-MoO$_3$. *J. Eur. Ceram. Soc.* **38**, 1541–1547 (2018).
26. Kumar, V. *et al.* Topotactic phase transformation of hexagonal MoO$_3$ to layered MoO$_3$-II and its two-dimensional (2D) nanosheets. *Chem. Mater.* **26**, 5533–5539 (2014).
27. Ji, F. *et al.* 2D-MoO$_3$ nanosheets for superior gas sensors. *Nanoscale* **8**, 8696–8703 (2016).
28. Hu, H., Deng, C., Xu, J., Zhang, K. & Sun, M. Metastable h-MoO$_3$ and stable α-MoO$_3$ microstructures: Controllable synthesis, growth mechanism and their enhanced photocatalytic activity. *J. Exp. Nanosci.* **10**, 1336–1346 (2015).
29. Song, Y., Zhao, Y., Huang, Z. & Zhao, J. Aqueous synthesis of molybdenum trioxide (h-MoO$_3$, α-MoO$_3$· H$_2$O and h-/α-MoO$_3$ composites) and their photochromic properties study. *J. Alloys Compd.* **693**, 1290–1296 (2017).
30. Ge, H., Kuwahara, Y. & Yamashita, H. Development of defective molybdenum oxides for photocatalysis, thermal catalysis, and photothermal catalysis. *Chem. Commun.* **58**, 8466–8479 (2022).
31. Borgschulte, A. *et al.* Hydrogen reduction of molybdenum oxide at room temperature. *Sci. Rep.* **7**, 40761 (2017).
32. Bramhaiah, K., Singh, K. K. & John, N. S. Single sea urchin–MoO$_3$ nanostructure for surface enhanced Raman spectroscopy of dyes. *Nanoscale Adv.* **1**, 2426–2434 (2019).
33. Bai, H. *et al.* Direct growth of defect-rich MoO$_{3-x}$ ultrathin nanobelts for efficiently catalyzed conversion of isopropyl alcohol to propylene under visible light. *J. Mater. Chem. A* **4**, 1566–1571 (2016).
34. Chiang, T. H. & Yeh, H. C. The synthesis of α-MoO$_3$ by ethylene glycol. *Materials* **6**, 4609–4625 (2013).
35. Bai, S. *et al.* Ultrasonic synthesis of MoO$_3$ nanorods and their gas sensing properties. *Sens. Actuators B Chem.* **174**, 51–58 (2012).
36. Salkar, A. V. *et al.* 2D α-MoO$_{3-x}$ truncated microplates and microdisks as electroactive materials for highly efficient asymmetric supercapacitors. *J. Energy Storage* **48**, 103958 (2022).
37. Chen, S., Xiong, F. & Huang, W. Surface chemistry and catalysis of oxide model catalysts from single crystals to nanocrystals. *Surf. Sci. Rep.* **74**, 100471 (2019).
38. Patil, M. K., Gaikwad, S. H. & Mukherjee, S. P. Phase-and morphology-controlled synthesis of tunable plasmonic MoO$_{3-x}$ nanomaterials for ultrasensitive surface-enhanced Raman spectroscopy detection. *J. Phys. Chem. C* **124**, 21082–21093 (2020).
39. Zu, D. *et al.* Oxygen-deficient metal oxides: Synthesis routes and applications in energy and environment. *Nano Res.* **12**, 2150–2163 (2019).
40. Jiang, J., Xu, T., Lu, J., Sun, L. & Ni, Z. Defect engineering in 2D materials: Precise manipulation and improved functionalities. *Research* **2019**, 4641739 (2019).
41. Dobrovolsky, A., Merdasa, A., Unger, E. L., Yartsev, A. & Scheblykin, I. G. Defect-induced local variation of crystal phase transition temperature in metal-halide perovskites. *Nat. Commun.* **8**, 34 (2017).
42. Lee, S. A. *et al.* Phase transitions via selective elemental vacancy engineering in complex oxide thin films. *Sci. Rep.* **6**, 23649 (2016).
43. Akın, Ü. & Şafak, H. Thickness dependence of dispersion parameters of the MoOx thin films prepared using the vacuum evaporation technique. *J. Alloys Compd.* **647**, 146–151 (2015).
44. Rouhani, M. *et al.* Photochromism of amorphous molybdenum oxide films with different initial Mo^{5+} relative concentrations. *Appl. Surf. Sci.* **273**, 150–158 (2013).
45. Anwar, M. & Hogarth, C. A. Optical properties of amorphous thin films of MoO$_3$ deposited by vacuum evaporation. *Phys. Status Solidi (A)* **109**, 469–478 (1988).
46. Xu, M.-F. *et al.* A comprehensive comparison of transition metal oxide MoO$_3$ and non-transition metal oxide GeO$_2$ in solar cells. *Appl. Phys. A* **124**, 1–5 (2018).
47. Zhang, C., Liu, G., Geng, X., Wu, K. & Debliquy, M. Metal oxide semiconductors with highly concentrated oxygen vacancies for gas sensing materials: A review. *Sens. Actuators A Phys.* **309**, 112026 (2020).
48. Yuan, H. *et al.* ZnO nanosheets abundant in oxygen vacancies derived from metal-organic frameworks for ppb-level gas sensing. *Adv. Mater.* **31**, 1807161 (2019).
49. Fjellvåg, Ø. S., Ruud, A., Sønsteby, H. H., Nilsen, O. & Fjellvåg, H. Crystallization, phase stability, and electrochemical performance of β-MoO$_3$ thin films. *Cryst. Growth Des.* **20**, 3861–3866 (2020).
50. Ma, M. *et al.* Oxygen vacancy engineering and superior sensing properties of hematite prepared via a one-step treatment. *Sens. Actuators B Chem.* **339**, 129907 (2021).
51. Yang, J. *et al.* Creating oxygen-vacancies in MoO$_{3-x}$ nanobelts toward high volumetric energy-density asymmetric supercapacitors with long lifespan. *Nano Energy* **58**, 455–465 (2019).
52. Wang, L., Zhang, G.-H., Sun, Y.-J., Zhou, X.-W. & Chou, K.-C. Preparation of ultrafine β-MoO$_3$ from industrial grade MoO$_3$ powder by the method of sublimation. *J. Phys. Chem. C* **120**, 19821–19829 (2016).
53. Lei, Z. *et al.* Recent advances of layered-transition metal oxides for energy-related applications. *Energy Storage Mater.* **36**, 514–550 (2021).
54. Guo, Y., Xu, K., Wu, C., Zhao, J. & Xie, Y. Surface chemical-modification for engineering the intrinsic physical properties of inorganic two-dimensional nanomaterials. *Chem. Soc. Rev.* **44**, 637–646 (2015).
55. Brachmann, E., Seifert, M., Oswald, S., Menzel, S. B. & Gemming, T. Evaluation of surface cleaning procedures for CTGS substrates for SAW technology with XPS. *Materials* **10**, 1373 (2017).
56. de Menezes Atayde, C. & Doi, I. Highly stable hydrophilic surfaces of PDMS thin layer obtained by UV radiation and oxygen plasma treatments. *Phys. Status Solidi C* **7**, 189–192 (2010).
57. Lo, M. F., Ng, T. W., Mo, H. W. & Lee, C. S. Direct threat of a UV-ozone treated indium-tin-oxide substrate to the stabilities of common organic semiconductors. *Adv. Funct. Mater.* **23**, 1718–1723 (2013).
58. Kumar, N. *et al.* Influence of the substrate temperature on the structural, optical, and electrical properties of tin selenide thin films deposited by thermal evaporation method. *Cryst. Res. Technol.* **45**, 53–58 (2010).
59. Kumar, N. *et al.* Structure, optical and electrical characterization of tin selenide thin films deposited at room temperature using thermal evaporation method. *J. Nano- Electron. Phys. SumDU* **3**, 117–126 (2011).

Acknowledgements

Author contributions

Competing interests

The authors declare no competing interests.

Additional information

Supplementary Information The online version contains supplementary material available at https://doi.org/10.1038/s41598-024-69765-x.

Correspondence and requests for materials should be addressed to K.N.A.S., L.K., K.M. or C.K.

Reprints and permissions information is available at www.nature.com/reprints.

Publisher's note Springer Nature remains neutral with regard to jurisdictional claims in published maps and institutional affiliations.